MICROCOPY RESOLUTION TEST CHART

NATIONAL BUREAU OF STANDARDS-1963-A

Final Report

Laser Remote Sensing of Atmospheric Pollutants

30 September 1982

MASSACHUSETTS INSTITUTE OF TECHNOLOGY

LINCOLN LABORATORY

LASER REMOTE SENSING
OF ATMOSPHERIC POLLUTANTS

D.K. KILLINGER
N. MENYUK
A. MOORADIAN

Group 82

FINAL REPORT
TO THE
AIR FORCE ENGINEERING AND SERVICES CENTER

1 OCTOBER 1981 — 30 SEPTEMBER 1982

ISSUED 9 MAY 1983

LEXINGTON   MASSACHUSETTS

Contents

Accession For

NTIS GRA&I
DTIC TAB
Unannounced
Justification

By
Distribution/

Availability Codes

Dist   Avail and/or
        Special

A

DTIC
COPY
INSPECTED
3

iii

I. INTRODUCTION

This is the FY82 final report on the program entitled "Laser Remote Sensing of Atmospheric Pollutants" supported by the Air Force Engineering and Services Center (AFESC). The effort is part of a larger ongoing program at Lincoln Laboratory to develop laser remote sensing techniques for the detection of chemical species in the atmosphere. Previous research for AFESC is documented in the FY79, FY80, and FY81 Final Reports.[1-3]

The specific tasks which were conducted during FY82 for this research program consisted of the following: (1) the initial development of a heterodyne-detection, differential-absorption LIDAR (DIAL) system, (2) the development of a computerized data acquisition and processing system for range-resolved, heterodyne-detection DIAL measurements, (3) preliminary range-resolved, heterodyne-detection DIAL measurements of atmospheric species, and (4) a study of the potential application of the continuously tunable $Co:MgF_2$ IR laser for remote sensing of airfield pollutants and gaseous species.

Each of the tasks are described in detail in the following sections. Supportive documentation is included in the appendices.

II. INITIAL DEVELOPMENT OF HETERODYNE-DETECTION DIAL SYSTEM

The direct-detection 10 μm dual-laser DIAL system as described in Ref. 3 was modified to permit operation with both direct detection and heterodyne detection. A schematic of the DIAL system is shown in Fig. 1 and a photograph of the system is presented in Fig. 2. Two grating-tuned nonstabilized hybrid-TEA CO_2 lasers provided pulsed, tunable, single-frequency radiation near 10 μm. The outputs from these two lasers were directed out the laboratory window and the LIDAR returns collected with a telescope. Through use of a beam splitter, the individual pulsed LIDAR returns could be detected simultaneously
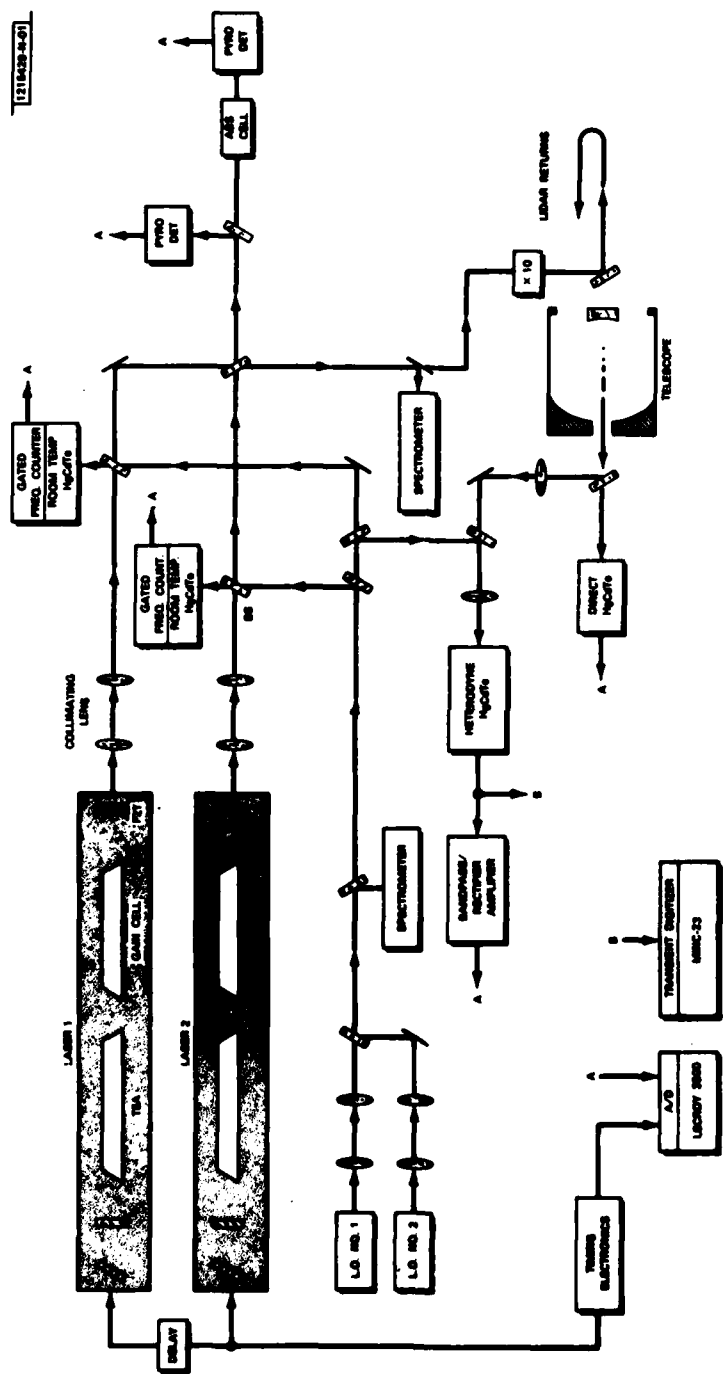
1

Fig. 1.   Schematic of heterodyne-detection and direct-detection CO_2 DIAL system.
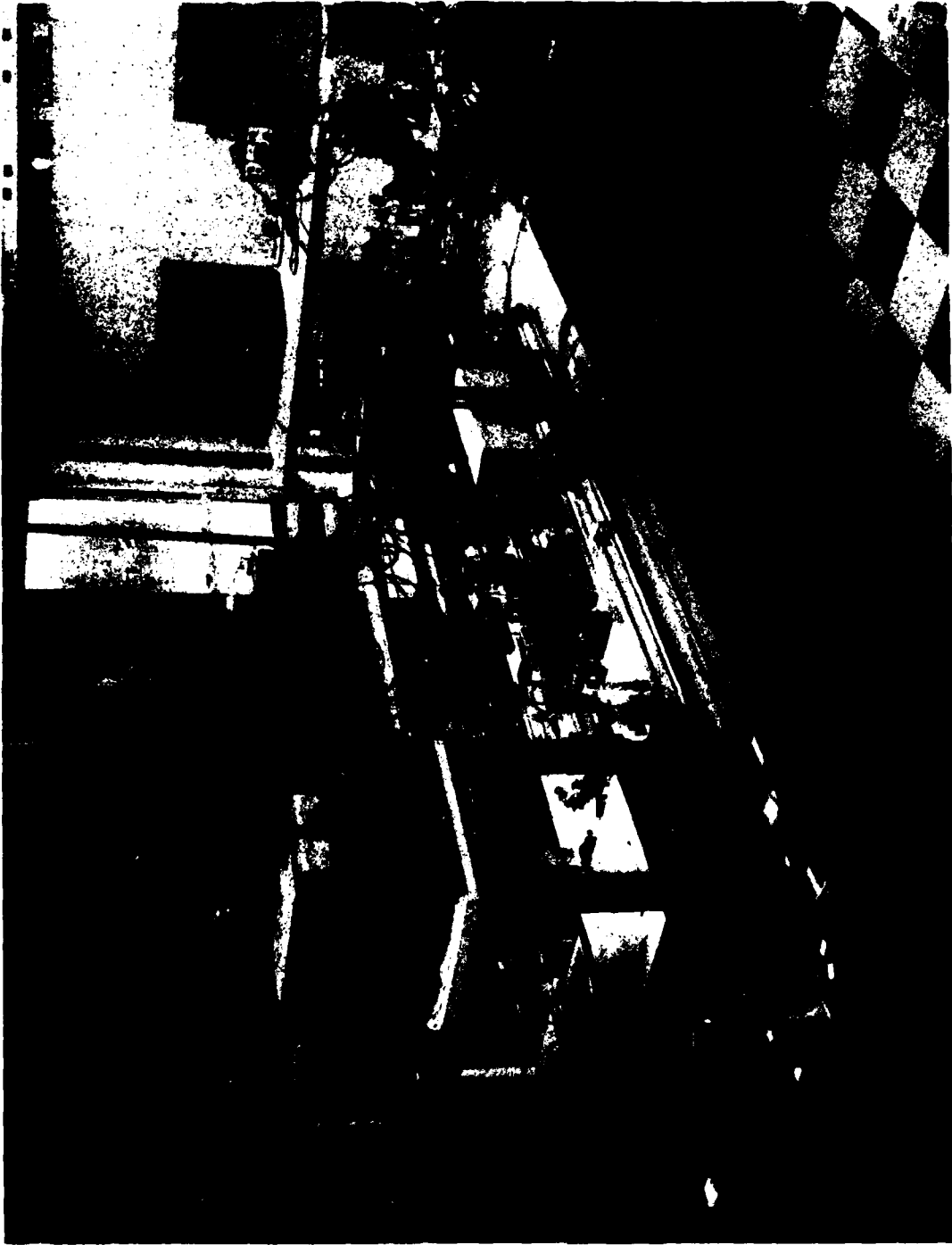
2

Fig. 2. Photograph of DIAL system.

both coherently (heterodyne detection) and noncoherently (direct detection). Appropriate power normalization, frequency monitoring, and signal processing were conducted as shown in Fig. 1. This system permitted the direct comparison of the signal-to-noise ratios and the statistical characteristics of direct and heterodyne detection of the same LIDAR returns.

LIDAR returns were recorded from several diffuse targets and specular retroreflectors at ranges up to 2.7 km. A statistical analysis of these signals was used to quantify the relative merits of the two detection techniques. The results are given in detail in Appendices A and B. A synopsis of the results is given below.

The heterodyne-detection DIAL system was found to have a higher average signal-to-noise ratio (SNR) than that of the direct-detection system, at the expense, however, of less accuracy in the remote sensing measurements at closer ranges. These differences are due to atmospheric and target speckle induced fluctuations in the LIDAR returns and the different ability of each detection system to compensate for these fluctuations. The results can be summarized as follows:

1. For the nonoptimized DIAL system used, the average SNR of the heterodyne system was a factor of 1,000 greater than that of the direct-detection system; these results agreed with theoretical prediction. It is anticipated, however, that this factor would be much lower (~10 to 100) for an optimized detection system.[4]

2. The accuracy of the DIAL measurements was approximately 3% for the direct-detection system and 20% for the heterodyne-detection system. These results reflect the greater fluctuation level of

4

the LIDAR returns measured with the heterodyne system due to speckle. The direct-detection system is capable of speckle or aperture averaging of the returns, thereby reducing the magnitude of the fluctuations.

3. The ability of each detection technique to compensate for the fluctuations through signal averaging is limited by changes in the physical characteristics of the atmosphere. These changes were observed to be the limiting factor in determining the measurement accuracy.

4. Of importance was the observation that the accuracy of the measurements did not improve as the square root of the number of LIDAR pulse averaged, but saturated at a level determined by the observed atmospheric drifts. These results agreed with theory, as presented in Appendix B.

5. The experimental results were used along with appropriate analysis to quantitatively predict the accuracy of laser remote sensing for both range-resolved and path-averaged measurements. An example of such a prediction is shown in Fig. 3, which illustrates the trade-offs of the increased signal strength coupled with increased fluctuations of the heterodyne system compared to the increased accuracy but shorter detection ranges of the direct-detection system for a given laser pulse energy.

The results give quantitative values for the sensitivity and accuracy of these DIAL measurements and provide insight into the physical processes which limit each of the two detection techniques.
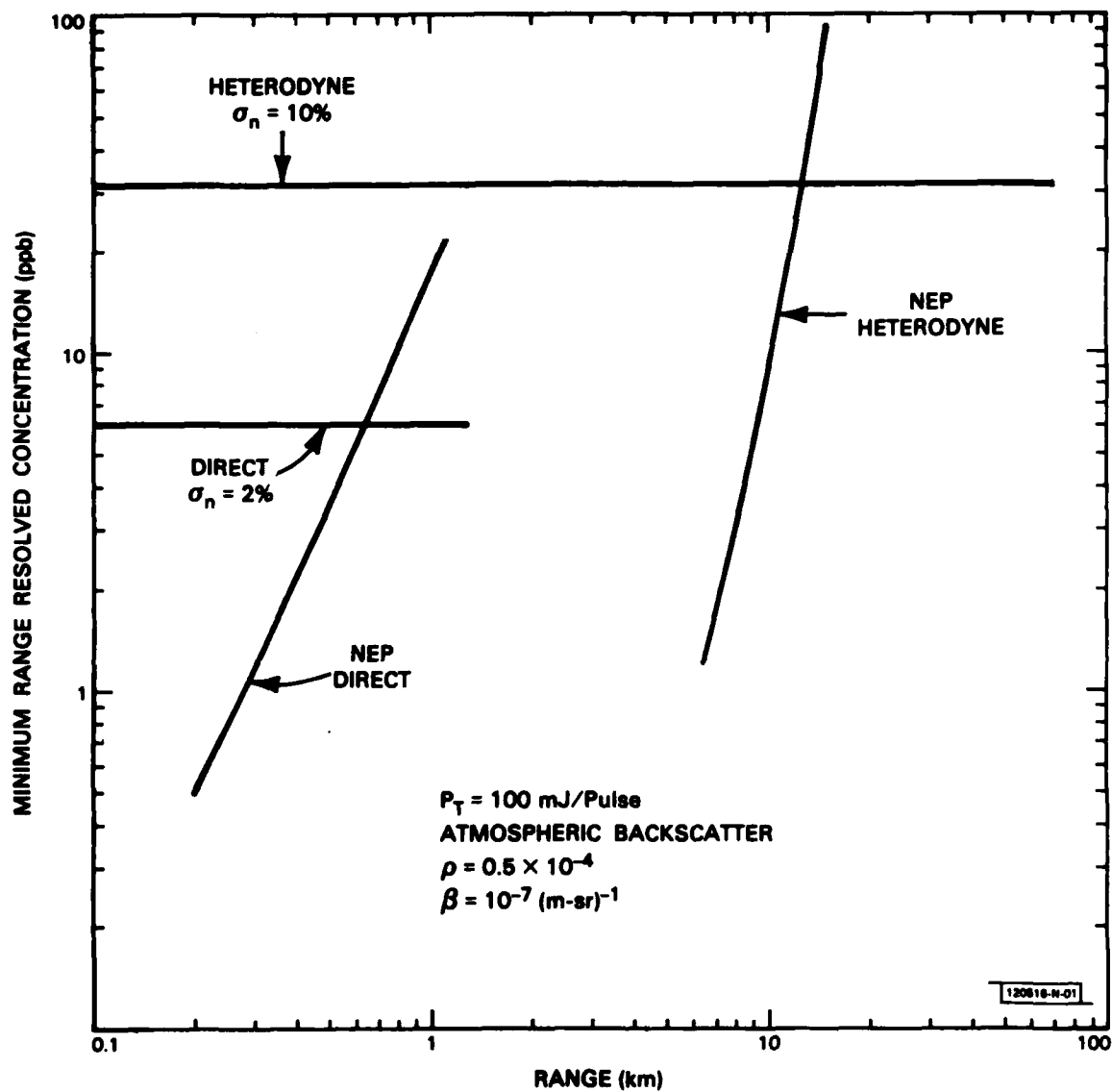
Fig. 3. Predicted detection sensitivity for CO_2 DIAL system.

III. DEVELOPMENT OF COMPUTERIZED DATA ACQUISITION AND PROCESSING SYSTEM

   FOR HETERODYNE-DETECTION DIAL SYSTEM

A computerized data acquisition and processing system was developed for use with the heterodyne-detection DIAL system. Two systems were developed for this purpose. The first system was a modified version of the previously used system[3] and consisted of a data acquisition system (computer, CAMAC crate, and A/D converters); this system was used to collect and analyze the pulsed LIDAR returns. The second system was comprised of a computer interfaced to a CAMAC crate and transient digitizer; this system recorded the transient waveform of the LIDAR returns. Both of these systems were capable of analyzing the data in real time at laser pulse-repetition-rates of up to 50 to 100 Hz. Typical analysis included the calculation of the SNR ratio, the statisticalcharacteristics of the heterodyne and direct-detection returns, and the concentration of the absorbing species.

IV. PRELIMINARY RANGE-RESOLVED, HETERODYNE-DETECTION DIAL

   MEASUREMENTS OF ATMOSPHERIC SPECIES

Preliminary range-resolved heterodyne LIDAR measurements were performed. These measurements consisted of detecting the 10.57-μm P(18) CO_2 LIDAR returns backscattered from atmospheric aerosols. Typical results are shown in Figs. 4 and 5 which show the return LIDAR signal as a function of time after integrating 128 pulses; Fig. 4 shows the background signal when the beam was blocked and Fig. 5 shows the increased signal due to the aerosol backscattered returns.
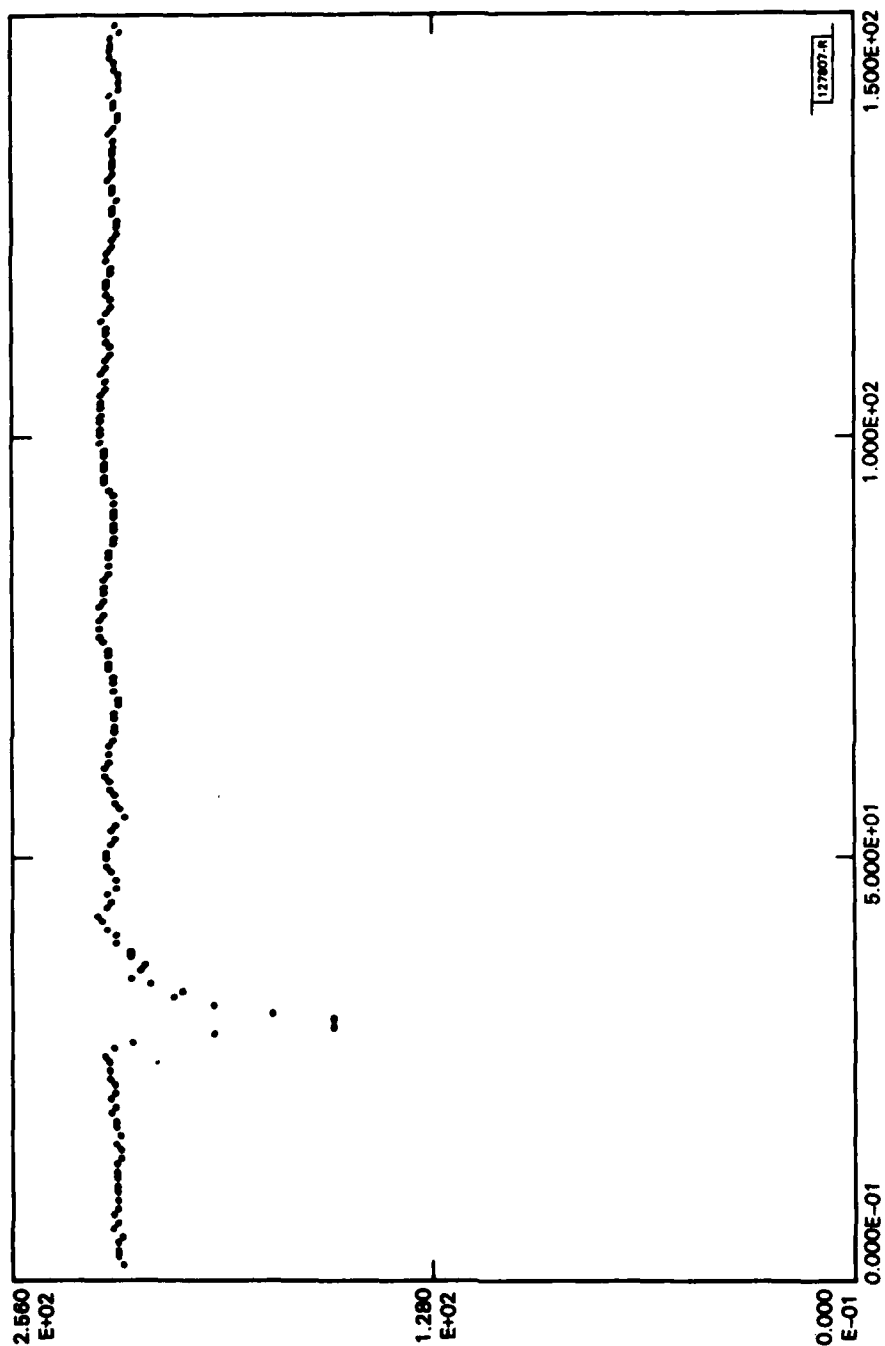
Fig. 4. Range-resolved LIDAR signal as a function of time with laser beam blocked: the time scale is in units of 50 ns.
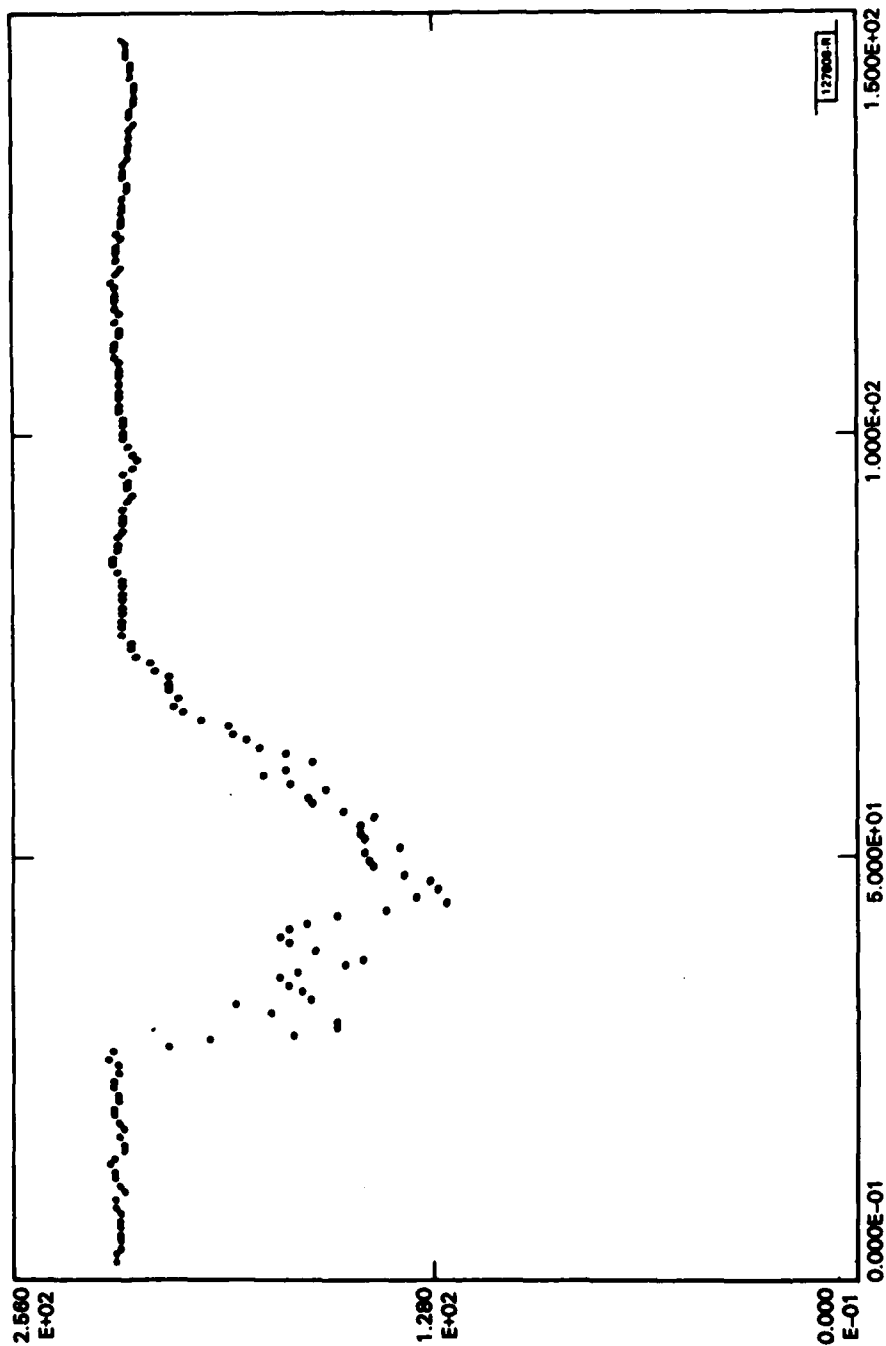
8

Fig. 5. Range-resolved atmospheric aerosol LIDAR signal as a function of time for 128 returns integrated: time scale is in units of 50 ns.

As seen in Fig. 5, returns were obtained at ranges out to approximately 500 meters (i.e., 3.3 μs). The returns, however, were observed to depend strongly on the focus and geometrical overlap of the projected LIDAR beam and the receiver (telescope) field of view. Such an effect directly influences the range dependence of the LIDAR returns. Preliminary studies were made into possible modification of the transmitter/receiver optical design; by proper alignment and focus, returns out to 1200 m were obtained, at the expense, however, of reduced returns at close in ranges. These studies pointed toward the requirement that a common transmitter/receiver telescope should be used for range-resolved LIDAR measurements at close ranges in order to ensure that both optical systems are focused at the same range and have maximal overlap of their two fields of view. Further work will be conducted in order to maximize this overlap with the present DIAL optical system.

V. STUDY OF THE POTENTIAL APPLICATION OF $Co:MgF_2$ LASERS FOR REMOTE SENSING

The transition-metal-doped solid-state laser, $Co:MgF_2$, has been developed at Lincoln Laboratory[5] and is a potential laser source for laser remote sensing. Previous work with the $Co:MgF_2$ laser has resulted in the growth of large $Co:MgF_2$ crystals, the operation of a cw $Co:MgF_2$ laser, and recently, high-power pulsed operation.

The $Co:MgF_2$ laser is continuously tunable over a wide spectral region in the range of 1.6 to 2.3 μm. In addition, through the use of frequency shifting techniques, this frequency region may be extended into the visible as well as mid-IR. Figures 6 and 7 show the anticipated tuning ranges of the $Co:MgF_2$ laser superimposed on the transmission spectrum of the atmosphere. The

10
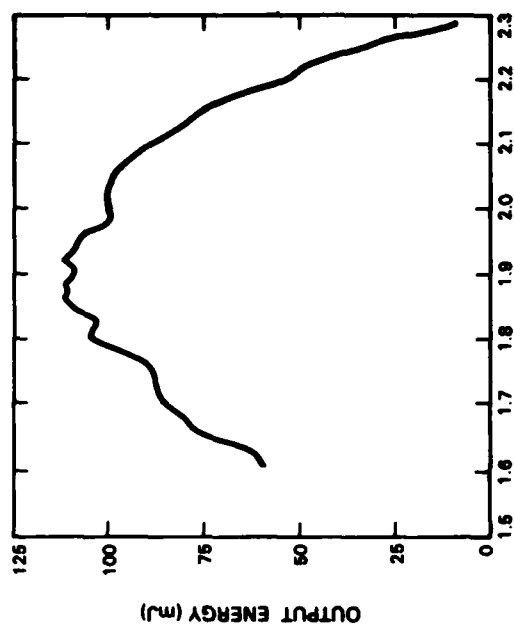
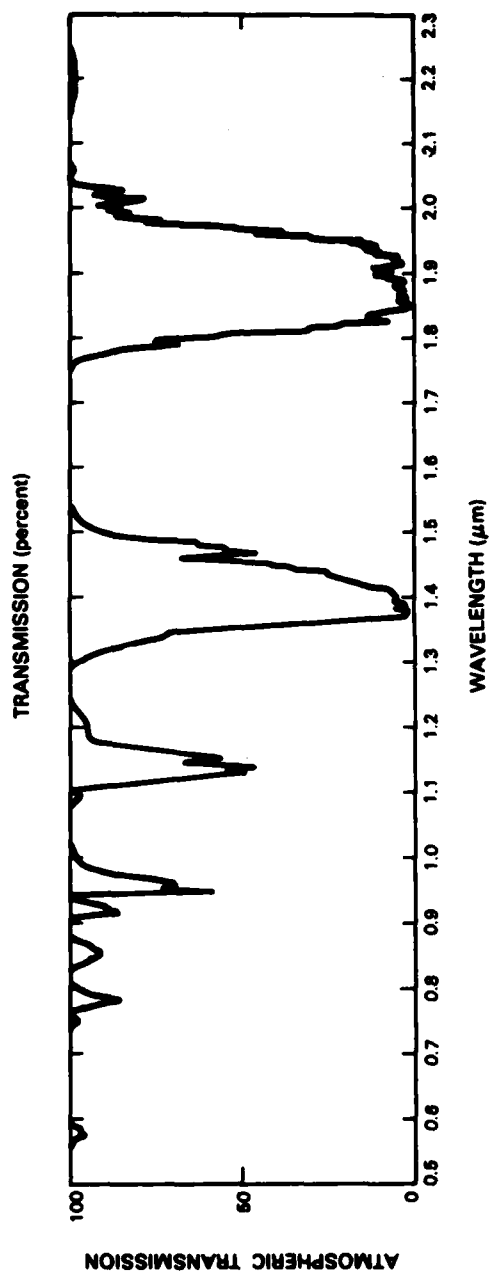Fig. 6.   Tuning ranges possible with harmonic generation of Co:MgF$_2$ laser.
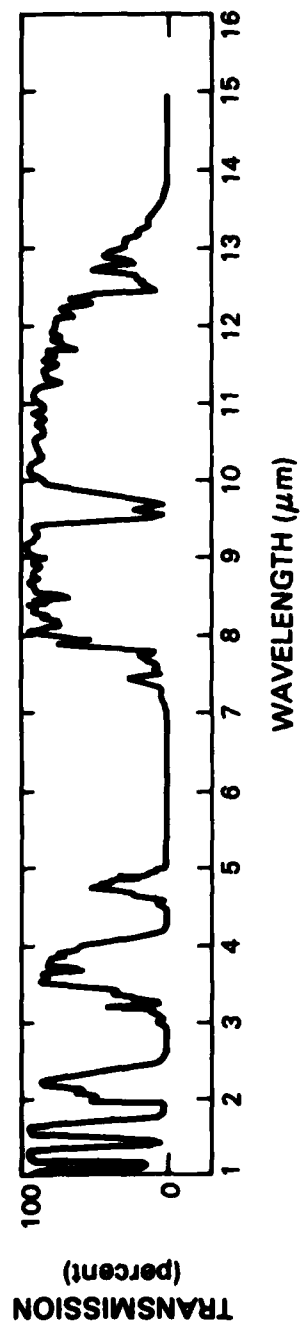
Fig. 7. Tuning ranges possible with frequency-downshifted Co:MgF₂ laser.

12

Co:MgF$_2$ is seen to potentially offer a wide range of spectral coverage not presently available with any other single-laser source.

In order to assess the potential usefulness of the Co:MgF$_2$ laser for remote sensing, a pulsed, Q-switched, tunable Co:MgF$_2$ DIAL system has been constructed. Figure 8 is a photograph of this system. Preliminary results have been obtained so far, and the results are encouraging.

At present, output power in the range of 100 mJ per pulse has been obtained when the laser is free-running, and 10 to 20 mJ when Q-switched. The Q-switched output pulse length is approximately 300 ns and the linewidth is approximately 0.15 cm^{-1}. These results were obtained with a single-element birefringent tuning filter and a 1-mm-thick uncoated etalon in the cavity. However, frequency pulling effects were observed when the laser was tuned away from the peaks of the Co:MgF$_2$ gain curve. The use of a triple-element birefringent tuning filter and coated etalon should help stabilize the spectral output of the laser.

Future work will further investigate the frequency stability of the Co:MgF$_2$ laser and test its usefulness for the remote sensing of selected species in the atmosphere.

VI. CONCLUSIONS AND RECOMMENDATIONS

The results presented in this report have described the capability of a CO$_2$ DIAL system for the remote sensing of species in the atmosphere. The differences between heterodyne detection and direct detection have been experimentally determined, and the accuracy of each system has been shown experimentally to be dependent upon several factors including atmospheric effects and target characteristics. In summary, the direct-detection DIAL system offers

13

Fig. 8. Photograph of Q-switched, pulsed, tunable Co:MgF$_2$ DIAL system.

14

higher accuracy and lower system complexity at the expense of shorter detection range, while the heterodyne-detection system has greater detection range at the expense of lower accuracy and greater system complexity.

A Co:MgF$_2$ DIAL system has been developed; preliminary results are encouraging since they indicate that this system will prove useful for the remote sensing and identification of species in the atmosphere. Further work to assess its capabilities is being conducted.

REFERENCES

1. A. Mooradian, D. K. Killinger, and N. Menyuk, "Remote Sensing of Turbine Engine Gases", Final Report, Lincoln Laboratory, M.I.T. (30 September 1979), ESD-TR-79-319/ESL-TR-80-09, DTIC AD-A084544/6.

2. D. K. Killinger, N. Menyuk, and A. Mooradian, "Remote Sensing of Turbine Engine Gases", Final Report, Lincoln Laboratory, M.I.T. (30 September 1980), ESD-TR-81-41/ESL-TR-81-16, DTIC AD-A099638.

3. D. K. Killinger, N. Menyuk, and A. Mooradian, "Remote Sensing of Turbine Engine Gases", Final Report, Lincoln Laboratory, M.I.T. (30 September 1981), ESD-TR-82-014/ESL-TR-82-016, DTIC AD-A115443.

4. D. L. Spears, "IR Detectors: Heterodyne and Direct", in Optical and Laser Remote Sensing (Springer-Verlag, 1983).

5. P. F. Moulton, "Pulse-Pumped Operation of Divalent Transition-Metal Lasers", IEEE J. Quantum Electron. QE-18, 1185 (1982).

Appendix A

The following is a reprint of a journal article published in Applied Optics, 1 March 1983, entitled "Experimental Comparison of Heterodyne and Direct Detection for Pulsed Differential Absorption CO_2 LIDAR".

Experimental comparison of heterodyne and direct detection for pulsed differential absorption CO$_2$ lidar

D. K. Killinger, N. Menyuk, and W. E. DeFeo

A pulsed dual-wavelength dual-CO$_2$-laser differential-absorption lidar (DIAL) system has been developed which permits simultaneous heterodyne and direct detection of the same lidar returns. This system has been used to make an experimental comparison of the SNRs and statistical and temporal characteristics of the DIAL returns from several topographic targets. These results were found to be in general agreement with theory and were used to quantify the relative merits of the two detection techniques. The measured parameter values were applied to an analytical treatment to predict system trade-offs for the remote sensing of atmospheric species, with application to both path-averaged and range-resolved measurements.

I. Introduction

The use of differential-absorption lidar (DIAL) systems with CO$_2$ laser sources has proven to be a sensitive method for achieving remote measurements of selected species in the atmosphere.[1] In general, most remote sensing measurements using CO$_2$ DIAL have been made using either pulsed CO$_2$ lasers in conjunction with direct (noncoherent) detection[2–4] or cw[5,6] and Q-switched cw[7] CO$_2$ lasers with heterodyne (coherent) detection. The advantages of using heterodyne detection with pulsed CO$_2$ DIAL have been studied theoretically[8–10] but have yet to be verified experimentally.

In this paper, an experimental comparison is made of the relative merits of heterodyne and direct detection. Measurements were made using a pulsed dual-wavelength dual-CO$_2$-laser differential-absorption lidar (DIAL) system which permitted simultaneous heterodyne and direct detection of the same lidar return. This system was utilized to obtain a direct experimental comparison of the SNRs and statistical and temporal characteristics of the DIAL returns. The results quantify the increase in the average detected lidar backscatter intensity relative to the average noise level for heterodyne compared with direct detection, and they provide a measure of the relative accuracy of the two detection techniques when applied to DIAL measurements.

A description of the experimental apparatus is given in Sec. II. Section III presents the experimental results which quantify the SNR, temporal correlation, and statistical fluctuation of the lidar returns; these results are shown to be in reasonable agreement with theory. The parameter values determined in Sec. III are used in an analytical treatment in Sec. IV to provide physical insight into the relative trade-offs between the two detection techniques. Finally, Sec. V presents an overview of the conclusions and experimental results.

II. Experimental Apparatus

A schematic of the dual-laser DIAL system is shown in Fig. 1. Two grating tuned nonstabilized hybrid-TEA CO$_2$ lasers provide the pulsed, tunable, single-frequency radiation near 10 μm. Each laser is similar to that reported previously[11,12] but with an additional 36-cm long low-pressure gain cell placed within the 1.32-m cavity; the low-pressure gain cell reduced the TEM$_{00}$ output linewidth of the laser from about four longitudinal modes to a single frequency. The output coupler is a 93% reflectivity 1.5-m radius-of-curvature mirror placed on a PZT mount. The TEA laser operated at a prf of up to 100 Hz. The output energy of the hybrid-TEA laser was ~10 mJ/pulse with a pulse length of 200 nsec. The low-pressure (10 Torr) gain cell was operated continuously at slightly above threshold, with an output power of 100 mW. No active or passive stabilization of the hybrid-TEA laser cavity was utilized except to mount the mirror components on large (15 × 15 × 15 cm) aluminum blocks. Laser 2 was fired a few μsec after laser 1 to provide temporal separation of the two pulses.

The frequency of each hybrid-TEA laser was adjusted to an offset frequency of ~20 MHz relative to that of a grating tuned, stable, 100-mW cw CO$_2$ laser local os-
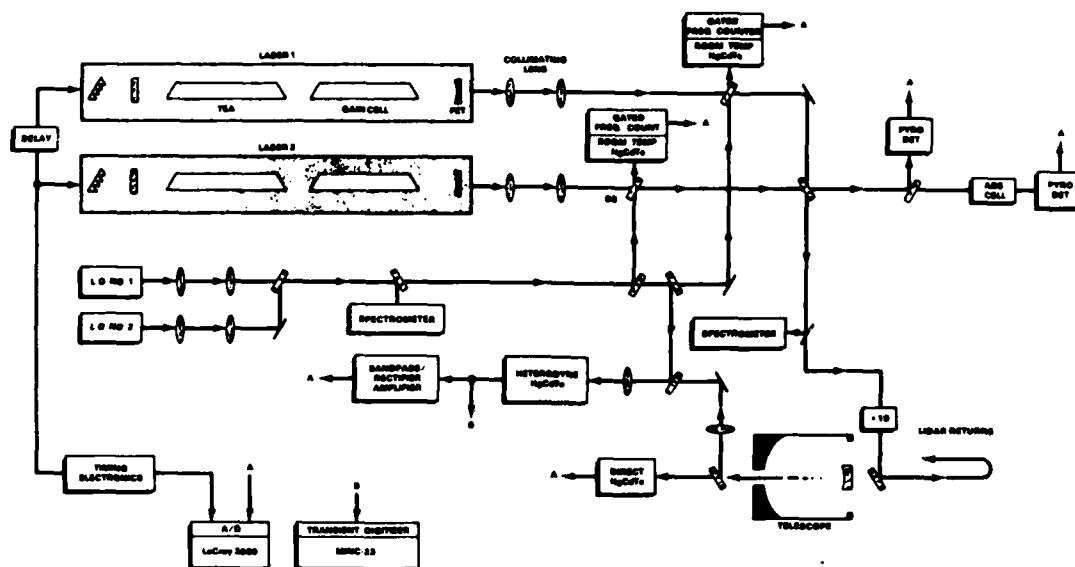
18

Fig. 1. Schematic of pulsed dual-wavelength dual-CO_2-laser differential-absorption lidar (DIAL) system providing simultaneous heterodyne and direct detection of the lidar returns.

cillator (LO); each LO had a frequency stability of better than 1 MHz. The stability of the hybrid-TEA laser compared to the LO frequency was monitored by measuring the heterodyne beat frequency using a room-temperature HgCdTe detector,[13] spectrum analyzer, and gated frequency counter. A 1-μsec gated frequency counter was used to monitor the beat frequency of the cw portion of the hybrid-TEA laser radiation just prior to the TEA pulse; a precision 100-nsec gated frequency counter was used to measure the frequency of the pulsed portion of the heterodyne beat frequency during the 200-nsec TEA pulse. These measurements established that the frequency of the pulsed portion of the hybrid-TEA laser output tracked the frequency of the cw portion within ±1 MHz. It was found that the pulse-to-pulse stability of the hybrid-TEA laser frequency was approximately ±5 MHz centered about the 20-MHz offset frequency, and the intrapulse frequency variation (chirp) was ~1 MHz. The TEA discharge disrupted the lasing of the cw gain cell because of the formation of contamination products; the time required to reestablish the cw lasing condition effectively limited the prf to ~100 Hz, dependent on discharge and gas-mixture conditions. It should be added that, while this simple-to-build hybrid-TEA laser does not offer the sub-MHz stability required for coherent Doppler measurements, its ±5 MHz stability is more than adequate for heterodyne detection.

The outputs of the two hybrid lasers were joined at a 50/50 beam splitter. Portions of the combined beams were sampled using beam splitters and pyroelectric detectors to measure the energy and absorption characteristics of each laser pulse against a known gas in a laboratory absorption cell. The laser beam was expanded by a ×10 beam expander to ~6–8 cm in diam-

eter and directed out the laboratory window toward topographic targets. The backscattered lidar radiation was collected using an $f/3$ Cassegrain telescope (variable 10–30-cm diam) and split into two beams with a 50/50 beam splitter. Half of the returned beam was detected by a cooled 1-mm diameter direct-detection photoconductive HgCdTe detector (NEP ~4 × 10^{-9} W), and the other half was mixed with the CO_2 local oscillator output and detected by a cooled 100-μm diam 1.5-GHz heterodyne-detection photovoltaic HgCdTe detector.[13]

The R.F. heterodyne signal was amplified using a low-noise 45-dB gain amplifier chain passed through a 50-MHz bandwidth filter, full-wave rectified using a R.F. transformer and zero-bias square-law Schottky detector diodes, envelope detected, and impedance matched with an emitter follower. The detector diodes were operated in the square-law region, where the output voltage is proportional to the square of the input voltage and not in the higher linear operating range.

The outputs from the HgCdTe detectors, frequency counters, and pyroelectric detectors were sent to a gated high-speed analog-to-digital data acquisition system. This system monitored the beat frequency (frequency offset) of each laser pulse to ensure that it fell within the limits of the 50-MHz bandpass filter, normalized the individual lidar returns to the transmitted laser pulse energy, and calculated the statistical and temporal characteristics of the returns in real time. In addition, a transient digitizer was used in conjunction with another computer to monitor the R.F. lidar return waveform for qualitative diagnostics. It should be noted that the real-time analysis of the data acquisition system (computational and graphical display) limited the effective prf of the lidar system to ~10–15 Hz.
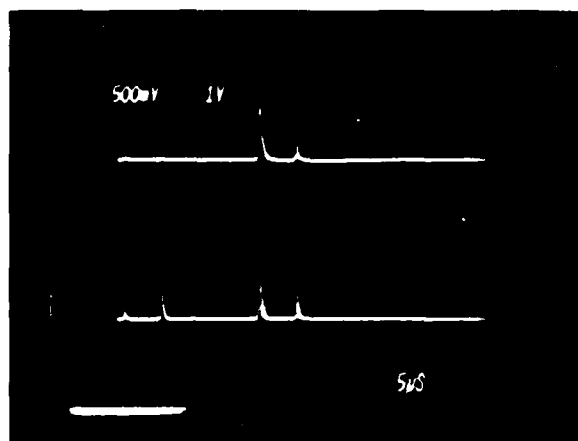
19

Fig. 2. CRT display showing dual-laser lidar returns from a target at a range of 2.7 km (time of flight of 17 μsec). Top trace is the direct-detection returns, and the bottom trace is the heterodyne-detection returns; the transmitted laser pulse at zero delay time is also evident in the bottom trace. Temporal separation between lasers 1 and 2 was 5 μsec.

Figure 2 is a photograph of a CRT display showing the simultaneous lidar returns using a diffuse target (flame-sprayed aluminum plate)[14] at a range of 2.7 km. The upper trace shows the direct-detection returns for lidars 1 and 2, and the lower trace shows the corresponding envelope-detected heterodyne returns. To properly compare the relative intensity of the returns for the two detection techniques, it should be noted that the current (and hence voltage output) for the direct-detection detector is proportional to the square of the received optical electric field, $E_R^* E_R$, which is the intensity of the received lidar return. For heterodyne detection, the output current of the HgCdTe detector at the beat frequency is proportional to the product of $E_R^* E_{LO}$, when E_{LO} is the optical electric field from the local oscillator.[15] The square-law detector chain is operated so that the output voltage V_0 is proportional to the square of the input voltage V_{IN}^2 so that $V_0 \propto V_{IN}^2 \propto E_R^2 E_{LO}^2$. Therefore, the voltage signals seen in Fig. 2 are proportional to the received lidar intensity for both direct and heterodyne detection.

III. Experimental Data

A. Average SNR of Lidar Returns

The average SNR of the lidar returns, which represents the ratio of the average intensity to the average noise, was measured for different targets at several ranges. Calibrated attenuators were used in the het-

erodyne-detection optical path to permit an accurate comparison of the two detection techniques. In general, the measured SNR value for the heterodyne-detected returns was found to be a factor of ~500–2000 greater than that for the direct-detected returns. As an example, using the side of a large, painted, corrugated metal building at a range of 2.7 km as a diffuse reflecting target, the direct-detection SNR was ~10, and the heterodyne-detection SNR after optical attenuation of 1000 was ~10 (i.e., SNR ~10,000). This observed difference in the measured SNR values may be compared with theory (valid for SNR ~1). The noise equivalent power (NEP) of the noncoherent detector is ~4 × 10^{-9} W. The noise of the heterodyne detector with sufficient local oscillator power is given[15] by

$$P_N \simeq h\nu B/\eta, \qquad (1)$$

where η is the quantum efficiency of the detector, and B is the bandwidth of the detector amplifier in hertz. Using typical values for our operating system of $\nu = 2.8 \times 10^{13}$ Hz, $\eta \sim 0.5$, and $B = 50$ MHz, Eq. (1) indicates a heterodyne-detection noise value of 2 × 10^{-12} W. The ratio of the estimated heterodyne-detection and the direct-detection noise value is ~2000 and in reasonable agreement with the observed experimental values for the ratio of the observed SNR values of 1000; this agreement is actually better than indicated since the experimental SNR was ~10.[13]

It is also instructive to compare the observed lidar return intensity with that predicted theoretically. The return lidar signal P_R is given[12] approximately by
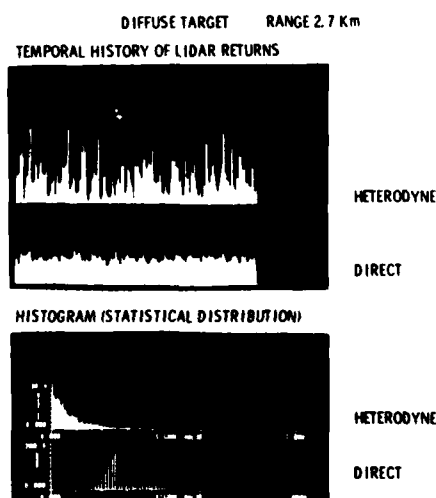

Fig. 3. Computer display showing temporal history and statistical distribution (histogram) of the lidar returns from a diffuse target (metal building) at a range of 2.7 km. The prf of the lidar was ~10 Hz.

20

Target	Heterodyne-detection lidar (%)	Direct-detection lidar (%)
Diffuse	100	20
Retroreflector	120	70

$$P_R = [P_T \rho A K \exp(-2\beta R)]/\pi R^2, \qquad (2)$$

where P_T is the transmitted laser power, ρ is the target reflectivity, A is the telescope collection area, K is the overall optical efficiency, β is the absorption coefficient of the atmosphere, and R is the lidar range. Typical estimated values for our lidar system are $P_T = 1$ mJ/100 nsec $= 10^4$ W, $\rho = 0.1$, $K = 0.1$, $A = 0.06$ m^2, and $\beta = 0.125$ km^{-1} at 10.52 μm. For a range of 2.7 km, Eq. (2) predicts a value for P_R of 1.4×10^{-7} W. Comparing this value as an estimate of the average signal return with the associated NEP, one estimates a SNR value of $(1.4 \times 10^{-7}$ W$)/(4 \times 10^{-9}$ W$) = 35$ for the direct-detection system and $(1.4 \times 10^{-7}$ W$)/(2 \times 10^{-12}$ W$) = 70,000$ for the heterodyne-detection system. Taking into account the order-of-magnitude estimates used in the analysis, the calculated values for SNR are in reasonable agreement with the experimental values of ~10 and 10,000, respectively. It should be noted that experiments which investigated the effect of the telescope aperture size on the return intensity indicated that the heterodyne signal increased by a factor of ~2 when the aperture was increased from 10 to 25 cm in diameter in agreement with recent theoretical prediction.[16]

B. Statistical Distribution

The standard deviation, temporal history, and statistical distribution of the lidar returns were recorded and differences observed and quantified between the heterodyne and direct-detection techniques. Figure 3 shows two photographs of the graphic display of the computerized data acquisition system. The upper photograph shows the temporal history of the simultaneous heterodyne and direct-detection 10-Hz prf lidar 1 returns from the sides of a large metal building at a range of 2.7 km. The lower photograph in Fig. 3 shows the statistical distribution (histogram) and related parameters of the lidar returns; similar results were observed for the corresponding return from laser 2 and also when a 1- × 1-m flame-sprayed aluminum plate was used as the diffuse target. As seen, the heterodyne returns have increased fluctuations due to speckle compared with the aperture-averaged direct-detection returns.

Figure 4 shows analogous results using a 1-in. diam retroreflector as the lidar target at a similar range. Differences between these results and those shown in Fig. 3 are evident. It should be noted that, for the case of the retroreflector returns shown in Fig. 4, attenuators were used to reduce the intensity of the outgoing lidar beam of the order of 10^3–10^5 so that the relative amplitudes of the signals shown in Figs. 3 and 4 were approximately the same.

The statistical distribution of the diffuse-target lidar returns in Fig. 3 is seen to approximate the expected negative exponential distribution for the heterodyne returns and appears to approximate a normal (Gaussian) distribution for the direct-detection returns.[17,19] The statistical distribution of the retroreflector returns in Fig. 4 for the heterodyne case appears to remain a negative exponential distribution; additional measurements, however, have shown different distributions under certain operating conditions.[20,21] The distribution for the direct-detection returns in Fig. 4 is seen to be similar to a lognormal distribution.

SPECULAR TARGET (1 in. RETRO)   RANGE 2.7 Km

TEMPORAL HISTORY OF LIDAR RETURNS

HETERODYNE

DIRECT

HISTOGRAM (STATISTICAL DISTRIBUTION)

HETERODYNE

DIRECT
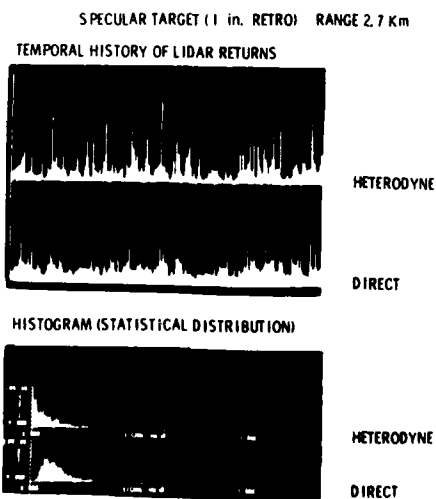
Fig. 4. Temporal history and statistical distribution of the lidar returns from a 1-in. retroreflector at a range of 2.7 km; prf ≈ 10 Hz.
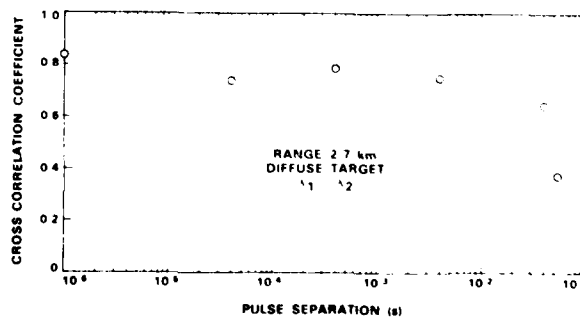
PULSE SEPARATION (s)

Fig. 5. Temporal pulse-pair cross-correlation coefficient as a function of pulse separation time between lasers 1 and 2 for heterodyne-detection lidar returns from a diffuse target at a range of 2.7 km. The wavelengths of the two lasers were the same, the P(20) line at 10.532 μm.

21

Target	Direct detection		Heterodyne detection	
	$\lambda_1 = \lambda_2$	$\lambda_1 \neq \lambda_2$	$\lambda_1 = \lambda_2$	$\lambda_1 \neq \lambda_2$
Diffuse	0.5	0.5	0.9	0.2[a]
Retroreflector	0.9	0.9	0.9	0.9

[a] Dependent on target surface roughness and $\lambda_1 - \lambda_2$; the value shown is for $\lambda_1 - \lambda_2 = 0.016\ \mu m$.

The statistical distributions shown in Figs. 3 and 4 are consistent with previously measured results for the direct-detection system as well as those predicted from theory and associated measurements for the heterodyne technique.[12,17,20] The exact distributions shown in Figs. 3 and 4 will have an influence on the accuracy of a DIAL measurement since they affect the standard deviation of the fluctuations. The standard deviation will influence the accuracy of a DIAL measurement since it determines the error in the estimate of the mean value of the lidar returns.

The measured standard deviation of the lidar returns for the two different targets at a range of 2.7 km is shown in Table I. As seen, the normalized standard deviation of the fluctuation in the lidar returns was found to be ~20% and 100% for the diffuse target returns and 70% and 120% for the 1-in. retroreflector return for direct detection and heterodyne detection, respectively; results obtained using the aluminum plate or the metal building as the diffuse target were essentially the same. These values are in order-of-magnitude agreement with theoretical predictions[22,23] and quantify the differences between the two detection techniques. Further analysis of these results will be presented in later sections.

C. Temporal Correlation

The temporal pulse-pair cross-correlation coefficient[24] ρ of the two return pulses for the two lasers was measured as a function of the temporal separation between the two laser pulses. The correlation coefficient is a measure of how well-correlated the fluctuations of lidar 1 returns are compared with the fluctuations of lidar 2 returns.

Figure 5 shows results obtained for the correlation coefficient of the dual-laser heterodyne returns from a diffuse target when the two laser wavelengths were the same. As seen, ρ is near unity at close separation times and falls off at typical atmospheric decorrelation times of the order of 10–50 msec.[24] The value of ρ at short (<50 μsec) delay times was found, however, to be dependent on the nature of the target, the relative wavelengths of the pulse pairs, and the type of detection system used. Table II shows typical approximate (± 0.1) values of ρ measured. It should be added that, while typical of our experimental conditions, the observed atmospheric decorrelation times shown in Fig. 5 are dependent, in general, on atmospheric conditions (wind speed, wind direction, and Cn^2 value), the dimensions of the transmit/receive optics, and the dynamics of the scattered far-field speckle pattern.[5,24]
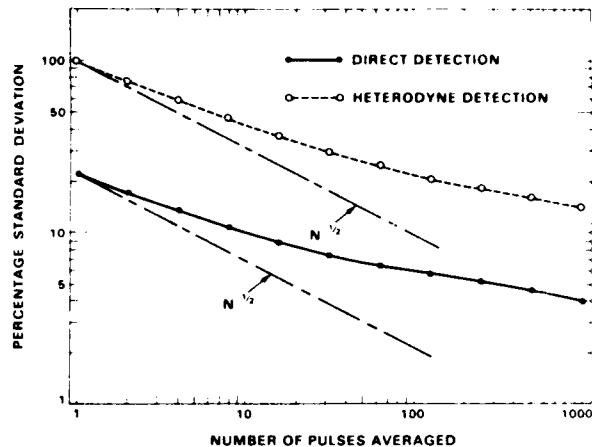

Fig. 6. Standard deviation in the estimate of the mean of the lidar returns as a function of the number of pulses integrated for returns from a diffuse target at a range of 2.7 km.

The value of ρ is seen in Table II to be large for retroreflector returns for all cases, including those in which the wavelength of the two lasers differed from each other by as much as 1 μm. This result is most probably due to the relative physical size of the retroreflector compared with the size of the modulated intensity patterns within the transmitted laser beam. One estimates that under the conditions of our experiments, the size of the intensity modulations (i.e., coherence length) was ~10–50 cm.[22,25] In this case, the retroreflector is essentially sampling the modulated intensity patterns within the transmitted laser beam and, as expected, should not be a strong function of wavelength or of the detection technique.

The results for the diffuse target show, however, strong dependence of the detection technique and of the laser wavelength separation. While the direct-detection results are consistent with previous results,[12,24] the heterodyne-detection results are notable for two reasons. First, the high value of ρ observed in Fig. 5 at short delay times indicates that the same interference or speckle pattern is being detected by both lidars 1 and lidar 2; the falloff of ρ at time separations of the order of 10–50 msec indicates that the detected speckle pattern is being modulated by atmospheric turbulence. Second, ρ is seen in Table II to be significantly reduced for heterodyne detection from a diffuse target case when λ_1 differs from λ_2 by as little as 0.016 μm, the difference between two adjacent CO_2 laser lines. This result is most probably due to the effect of decorrelation of the speckle pattern caused by the surface roughness of the target when the wavelength of the radiation is varied.[26] The functional relationship of ρ on surface roughness and wavelength may be expressed as $\rho = \exp[-(\Delta k \sigma_z/\sqrt{2})^2]$, where σ_z is the standard deviation of the surface roughness, and Δk is the difference in the laser frequencies.[26] As an order-of-magnitude estimate, one may take an estimated value of $\sigma_z = 2$ mm and $\Delta k \cong 2\pi\Delta\lambda/\lambda^2 = 0.00091\ (\mu m)^{-1}$. Using these
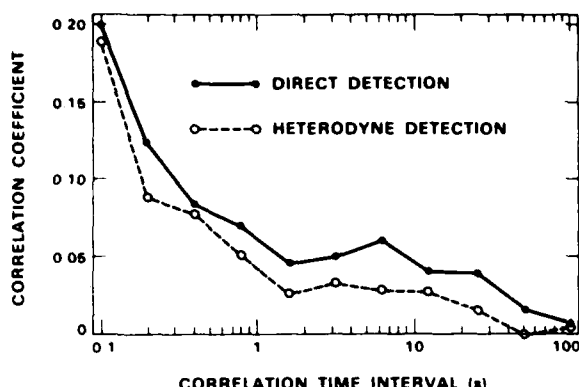
22

Fig. 7. Temporal autocorrelation coefficient of the lidar returns (prf ≈ 10 Hz) as a function of temporal separation between the measurements.
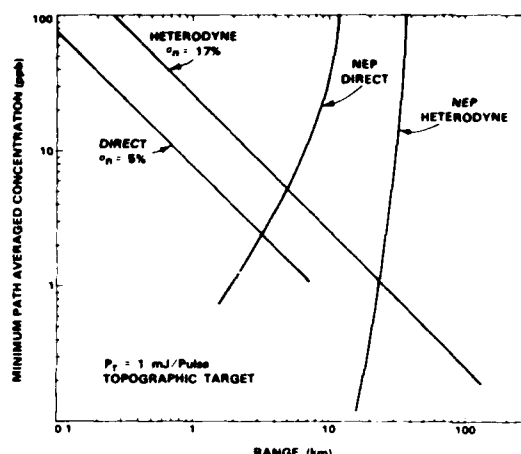

Fig. 8. Calculated minimum detectable path-averaged concentration of ethylene, N_{min}, as a function of range for heterodyne- and direct-detection DIAL.

values, one predicts a value of $\rho \sim 0.2$, in reasonable agreement with the observed value shown in Table II.

The above results obtained for the value of ρ for the two different detection techniques are of interest because they influence the degree to which the effect of the lidar return fluctuations can be reduced by the use of a dual-laser system.[27] In particular, the low value of ρ observed for the heterodyne and diffuse target case when $\lambda_1 \neq \lambda_2$ with the two wavelengths separated by as little as 0.016 μm implies that little reduction will be obtainable for such a DIAL system. The detailed implications of such effects will not be covered here but will be published in a later paper which will combine the effect of both cross-correlation and long-term atmospheric-induced effects on DIAL remote-sensing errors.[28]

D. Measurement Accuracy in Determination of Average Lidar Return

The accuracy of a laser remote-sensing measurement is related to the determination of the average value of the lidar return signal. Previous experiments using direct detection have shown the limitation imposed on the accuracy of such measurements by the atmospheric-turbulence-induced temporal correlation of the lidar returns.[12] To establish this relative accuracy for both heterodyne and direct detection, the standard deviation of the mean, σ_n,[29] of the lidar return was measured. Figure 6 shows the measured standard deviation of the mean value of the 10-Hz prf lidar returns as a function of the number of pulses integrated, n. As seen, σ_n, and hence the fluctuation-induced error of the direct-detection system, is lower than that for the heterodyne system, reflecting the decreased fluctuations in Fig. 3 and Table I.

The deviation from the expected square-root dependence on n, the number of pulses integrated, is due to the nonzero temporal autocorrelation of the returns.[30] Figure 7 shows the measured temporal autocorrelation

coefficient for the same data as in Fig. 6 and clearly indicates the nonrandom nature of the returns. It is interesting to note that both detection techniques display similar long-term correlation effects indicative of similar absorption or scattering properties of the atmosphere under these conditions. The results shown in Fig. 6 indicate an effective limit[30] to the improvement in the SNR (i.e., standard deviation of the mean) of the order of 6 or 7 for both the heterodyne- and the direct-detection cases under the conditions of our experiments. The implications of this on laser remote-sensing accuracy will be discussed in Sec. IV.

It should be added that the results shown in Figs. 5–7 are fairly typical results yet are indicative of the particular experimental conditions (atmosphere, range, system parameters) while the measurements were being made. In general, significant changes in the measured values of σ_n and ρ can occur over time periods as short as a few seconds to a few minutes (see Figs. 11 and 12 in Ref. 29).

IV. Comparison of DIAL Measurement Accuracy for Atmospheric Species

The previous sections presented experimental results which indicated the differences in the signal strength and fluctuation levels of the two detection techniques. In this section, these results will be used along with appropriate analysis to numerically predict the accuracy of a laser remote-sensing measurement for heterodyne detection and for direct detection.

Previous analysis has shown that the accuracy of a DIAL measurement may be limited by the effect of the fluctuations of the lidar returns at close-in ranges and by the noise of the detector at far ranges.[12,29] To express this limitation, one may relate the minimum path-averaged concentration of gas that can be detected, N_{min}, to the NEP of the detector as
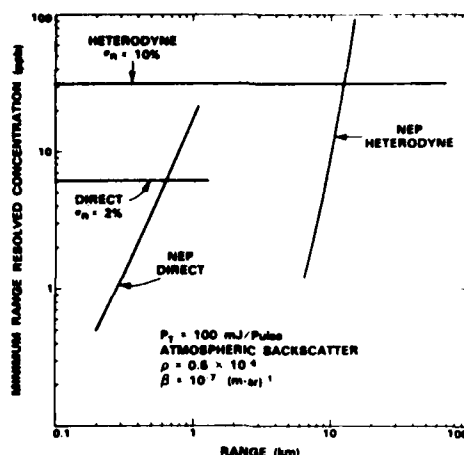
Fig. 9. Calculated minimum detectable range-resolved concentration of ethylene, N_{min}, as a function of range. Range resolution is 500 m.

$$N_{min} \simeq (NEP)\pi R/[2\rho\sigma_a KAP_T \exp(-2\beta R)], \qquad (3)$$

where σ_a is the absorption cross section of the gas.

The corresponding equation for the fluctuation-limited case is

$$N_{min} \simeq \sigma_n/(2\sigma_a R), \qquad (4)$$

where σ_n is the standard deviation of the mean value of the lidar returns.

Equations (3) and (4) may be used to compare the detection accuracy of both heterodyne- and direct-detection DIAL systems. As an example, one may use the same parameter values as those used earlier in Eq. (2). In addition, reasonable values for σ_n may be obtained from Fig. 6; for $n = 512$, $\sigma_n = 5\%$ and 17% for the direct and heterodyne cases, respectively. A nominal value for σ_a is 32×10^6 (km atm)$^{-1}$, representative of the absorption cross section of ethylene near 10.532 μm.[31]

Using these values in Eqs. (3) and (4), one obtains the curves shown in Fig. 8. The envelope of detection for each system is the area of the region bounded by the two detection limits for each system, respectively. As seen, at close-in ranges, the sensitivity or accuracy of the direct-detection DIAL system is better, while at long range, the increase in average SNR of the heterodyne system is responsible for the improved detectivity at these ranges. Figure 8 succinctly illustrates the appropriate trade-offs of the increased signal strength coupled with increased fluctuations of the heterodyne system compared to the increased accuracy but shorter detection ranges of the direct-detection system for a given laser pulse energy.

A similar analysis can also be applied to range-resolved DIAL measurements which utilize backscatter from aerosols in the atmosphere instead of topographic target returns. In this case, for a CO_2 lidar system which has sufficient sensitivity to detect backscatter from atmospheric aerosols, Eqs. (3) and (4) should be modified by replacing ρ with $(\beta'\Delta R)$ and σ_a with $(\sigma_a\Delta R/R)$, where ΔR is the range resolution of the system, and β' is the Mie backscatter coefficient. For the assumed values $P_T \sim 100$ mJ, $\rho \sim 0.5 \times 10^{-4}$ (for β' $= 10^{-7}$ m^{-1}-sr^{-1} and $\Delta R = 500$ m), $\sigma_n \sim 10\%$ and 2% for heterodyne[32] and direct detection,[33] respectively, for $n = 100$, and with the other parameter values taken to be the same as in the preceding example, the range-resolved detection curves shown in Fig. 9 are obtained. Figure 9 shows a detection envelope similar to that in Fig. 8, except that the close-in detection sensitivity is independent of range since Eq. (4) has been modified to $N_{min} \sim \sigma_n/(2\sigma_a\Delta R)$, and at the long ranges Eq. (3) has been modified to be proportional to $(NEP)R^2/$ $\exp(-2\beta R)$. In the latter case, the relative increase in detection range for heterodyne compared with direct detection is dominated by the $\exp(-2\beta R)$ term at very far ranges and the $1/R^2$ contribution at closer ranges; this is why the NEP curves for direct and heterodyne detection are not related to each other simply by the square root of the ratio of the respective NEP values in Fig. 9.

It should be noted that Eqs. (3) and (4) represent approximations and were presented to provide physical insight into the relative detection limits. In the more general case, the values of NEP and σ_n as well as the range dependence in Eqs. (3) and (4) would be dependent on several factors. These include the range dependence of the fluctuation or atmospheric turbulence levels,[20] aperture-averaging effects,[23] the use of cold interference filters and amplifiers to reduce the direct-detection NEP value,[13] the use of heterodyne detector arrays to reduce speckle-induced fluctuations,[34] increased signal averaging through the use of high-prf lasers,[22] and the trade-offs between the effects of short- and long-term temporal correlation for DIAL remote sensing of atmospheric species.[28] This latter consideration is expected to be important for range-resolved heterodyne detection of atmospheric aerosols; as an example, low short-term correlation values may drive

24

the system design toward the use of high-prf lasers in order to reduce the speckle-induced σ_n values under certain operating conditions. However, long-term temporal changes in the atmosphere may indicate the advantages of a dual-laser DIAL system in spite of low short-term cross-correlation.[28,29]

V. Conclusions

This paper has presented an overview of our CO_2 heterodyne- and direct-detection DIAL measurements. Using a relatively simple-to-build hybrid-TEA CO_2 laser, lidar returns have been detected simultaneously both coherently and noncoherently from several targets. The relative average SNR and fluctuation levels of the two systems were measured and found to qualitatively agree within factors of the order of unity with previous theoretical predictions. Finally, analytical equations were presented which related the detection sensitivity of the two systems as a function of range. The examples presented clearly indicate the sensitivity trade-offs of the two systems as a function of range and provide physical insight into the relative differences. It should be noted, however, that while the overall trade-off analysis as outlined in this paper shows the relative technical merits, other considerations such as system complexity should be considered for a complete system performance analysis.

References

1. R. L. Byer, Opt. Quantum Electron. 17, 147 (1975).
2. J. L. Bufton, R. W. Stewart, and C. Weng, Appl. Opt. 18, 3363 (1979).
3. E. R. Murray and J. E. van der Laan, Appl. Opt. 17, 814 (1978).
4. K. Asai, T. Itabe, and T. Igarashi, Appl. Phys. Lett. 35, 60 (1979).
5. M. S. Shumate, R. T. Menzies, W. B. Grant, and D. S. McDougal, Appl. Opt. 20, 545 (1981); R. T. Menzies and M. S. Shumate, Appl. Opt. 15, 2080 (1976).
6. W. Wiesemann, R. Beck, W. Englisch, and K. Gurs, Appl. Phys. 15, 257 (1977).
7. S. Lundqvist, C. O. Faelt, U. Persson, B. Marthinsson, and S. T. Eng, Appl. Opt. 20, 2534 (1981).
8. R. M. Hardesty, "A Comparison of Heterodyne and Direct Detection CO_2 DIAL Systems for Ground-Based Humidity Profiling," NOAA Tech. Memo. ERL-WPL-64, Oct. 1980.
9. P. Brockman, R. V. Hess, L. D. Staton, and C. H. Bair, "DIAL with Heterodyne Detection Including Speckle Noise," NASA Tech. Paper 1725, Aug. 1980.
10. B. J. Rye, Appl. Opt. 17, 3862 (1978).
11. N. Menyuk and P. F. Moulton, Rev. Sci. Instrum. 51, 216 (1980).
12. D. K. Killinger and N. Menyuk, IEEE J. Quantum Electron. QE-17, 1917 (1981).
13. D. L. Spears, Proc. Soc. Photo-Opt. Instrum. Eng. 300, 174 (1981); D. L. Spears, "IR Detectors: Heterodyne and Direct," Technical Digest of Workshop on Optical and Laser Remote Sensing, Monterey, 9–11 Feb. (1982).
14. R. A. Brandewie and W. C. Davis, Appl. Opt. 11, 1526 (1972).
15. R. H. Kingston, Detection of Optical and Infrared Radiation (Springer, New York, 1978).
16. J. Y. Wang, Appl. Opt. 21, 464 (1982).
17. R. M. Hardesty, R. J. Keeler, M. J. Post, and R. A. Richter, Appl. Opt. 20, 3763 (1981).
18. C. M. McIntyre, M. H. Lee, and J. H. Churnside, J. Opt. Soc. Am. 70, 1084 (1980).
19. J. F. Holmes, M. H. Lee, and J. R. Kerr, J. Opt. Soc. Am. 70, 355 (1980).
20. S. F. Clifford and R. J. Hill, J. Opt. Soc. Am. 71, 112 (1981).
21. E. Jakeman and P. N. Pusey, Phys. Rev. Lett. 40, 546 (1978).
22. J. H. Shapiro, B. A. Capron, and R. C. Harney, Appl. Opt. 20, 3292 (1981); J. H. Shapiro, "Target Detection with a Direct-Detection Optical Radar," Project Report TST-27, MIT Lincoln Laboratory, Nov. 1978, ADA No. 065 627.
23. For a negative exponential distribution, the value of the standard deviation equals that of the mean; therefore, the normalized standard deviation is 1. This is equivalent to the statement that the SNR = 1 since, as in Ref. (22), the voltage SNR may be defined as the ratio of the mean value divided by the standard deviation.
24. N. Menyuk and D. K. Killinger, Opt. Lett. 6, 301 (1981).
25. R. E. Hufnagel, "Propagation Through Atmospheric Turbulence," in The Infrared Handbook, W. L. Wolfe and G. J. Zissis, Eds. (Office of Naval Research, Washington, D.C., 1978), Chap. 6.
26. G. Parry, "Speckle Patterns in Partially Coherent Light," in Laser Speckle and Related Phenomena, J. C. Dainty, Ed. (Springer, New York, 1975), p. 100; N. George and A. Jain, Appl. Phys. 4, 201 (1974).
27. D. K. Killinger and N. Menyuk, Appl. Phys. Lett. 38, 968 (1981).
28. N. Menyuk, D. K. Killinger, and C. R. Menyuk (to be submitted for publication, Appl. Opt.)
29. N. Menyuk, D. K. Killinger, and W. E. DeFeo, Appl. Opt. 21, 2275 (1982).
30. N. Menyuk, D. K. Killinger, and C. R. Menyuk, Appl. Opt. 21, 3377 (1982).
31. A. Mayer, J. Comera, H. Charpenties, and C. Jaussaud, Appl. Opt. 17, 391 (1978).
32. R. J. Hull, MIT Lincoln Laboratory; private communication; CO_2 lidar range-resolved heterodyne detection of atmospheric aerosols.
33. J. L. Bufton, NASA Goddard; private communication; CO_2 lidar range-resolved direct detection of atmospheric aerosols.
34. Detector arrays may be used in heterodyne-detection lidar to reduce the effects of speckle-induced fluctuations. For the case of an optimized detection system as in Refs. 8 and 9, the reduction in σ_n^2 is predicted to be offset by a corresponding decrease in SNR; however, for a lidar system in which σ_n is dominated by atmospheric effects rather than being related to SNR, relative detection advantages can be gained from the use of a detector array.

Appendix B

    The following is a reprint of a journal article published in Applied
Optics, 15 September 1982, entitled "Limitations of Signal Averaging due to
Temporal Correlation in Laser Remote Sensing Measurements".

Limitations of signal averaging due to temporal correlation in laser remote-sensing measurements

N. Menyuk, D. K. Killinger, and C. R. Menyuk

Laser remote sensing involves the measurement of laser-beam transmission through the atmosphere and is subject to uncertainties caused by strong fluctuations due primarily to speckle, glint, and atmospheric-turbulence effects. These uncertainties are generally reduced by taking average values of increasing numbers of measurements. An experiment was carried out to directly measure the effect of signal averaging on backscattered laser return signals from a diffusely reflecting target using a direct-detection differential-absorption lidar (DIAL) system. The improvement in accuracy obtained by averaging over increasing numbers of data points was found to be smaller than that predicted for independent measurements. The experimental results are shown to be in excellent agreement with a theoretical analysis which considers the effect of temporal correlation. The analysis indicates that small but long-term temporal correlation severely limits the improvement available through signal averaging.

I. Introduction

The remote sensing of gaseous species in the atmosphere using a direct-detection differential-absorption lidar (DIAL) system requires the measurement of the average backscattered lidar return signals at both a high- and a low-absorption frequency of the species under investigation and a determination of their ratio. These measurements are subject to uncertainties caused by large fluctuations in the received signals due primarily to speckle, glint, and atmospheric-turbulence effects. The physics of laser-beam fluctuations in the atmosphere has been studied extensively by several authors,[1] with consideration given to both one-way laser propagation[2,3] and backscattered returns from remote targets.[4-6] These fluctuations frequently establish the limit of sensitivity by being the major cause of uncertainty in the average value of the lidar signals.

In this paper we shall be primarily concerned with determining the limitations that temporal correlation places on the ability of signal averaging to reduce this measurement uncertainty. It should be emphasized that this determination is independent of the origin of the fluctuations causing the uncertainty.

The measurement uncertainty is defined as the normalized standard deviation of the lidar signals. A standard technique for improving measurement accuracy is to increase the number of measurements and take the average value. For N measurements, the uncertainty is expected to decrease as $N^{-1/2}$, assuming that all the measurements are independent. An experiment was conducted which directly tested the validity of this assumption by measuring the standard deviation of lidar returns as a function of the number of pulses averaged. The reduction of the standard deviation by signal averaging was found to be much more weakly dependent on N than $N^{-1/2}$, indicating that the individual lidar measurements are not mutually independent. This lack of independence was established by an analysis of the data, which showed the presence of positive temporal correlation extending over time periods of several seconds to minutes for different data samples. This long-term correlation of the lidar returns is presumably due to slow changes in atmospheric absorption occurring during the measurement interval. Among the potential sources of such changes, including pressure, temperature, and aerosol variations, humidity fluctuations are believed to play the most significant role.

The experimentally observed variation of the standard deviation with the number of pulses averaged is shown to be in excellent agreement with a theoretical analysis which considers the temporal correlation of successive lidar returns. It should be noted that this theoretical analysis quantifies the deviation of any signal-averaging process from the $N^{-1/2}$ behavior due to nonrandom behavior and is, in general, applicable to a wide range of signal-averaging phenomena.

II. Experimental Results

The direct-detection dual-laser DIAL system used for this experiment has been described previously.[7,8] It employs two line-tunable mini-TEA CO_2 lasers[9] to provide the pulsed coherent radiation. The time delay between the firing of the two lasers was maintained at 50 μsec, so that the atmosphere may be considered frozen between firings.[7] A portion of each beam was sent to a pyroelectric detector to normalize the energy in each pulse, but the bulk of the radiation was directed outside the laboratory toward a 1- × 1-m flame-sprayed aluminum plate located at a range of 2.7 km which served as a diffusely reflecting target. The lidar returns were recorded and normalized in a computerized data-acquisition system.

For this experiment, laser 1 was fired on the 10.67-μm $P(28)$ CO_2 laser transition, and 50 μsec later laser 2 was fired on the 10.61-μm $P(22)$ transition. At these transition frequencies the atmospheric-transmission levels are high, with water vapor the primary source of atmospheric absorption.[10]

A total of 22,528 normalized lidar return pulses from each laser was recorded for later statistical analysis; the lidar return signals were normalized on a pulse-to-pulse basis to the energy in each transmitted pulse. The entire process took 40 min, corresponding to an overall pulse repetition frequency of slightly under 10 Hz. Computational constraints limited analysis to sets of 12,288 normalized pulse returns from each laser and their ratios. The initial and final sets of 12,288 pulses each exhibited somewhat differing behavior. Therefore, a full analysis was carried out for these two sets of data separately. It should be noted that there is an overlap in the data of the two sets; that is, the last 2048 pulses of the initial set correspond to the first 2048 pulses of the final set. With Γ defined as the total number of pulses in a data set (in the present case Γ = 12,288), statistical analysis of the two sets of lidar return data included a determination of the average value of each set of Γ returns, the standard deviation of the returns, and the normalized standard deviation of the average value of the returns, σ_N as a function of N, the number of pulses being averaged.

The standard deviation was determined using two distinct methods to define the mean values of the N pulses being integrated. The first method used a segmental-averaging approach. In this case, as an example, for N = 8, the segments averaged would be 1–8, 9–16, 17–24, . . . , 12,281–12,288, and the measured standard deviation of the mean is based on the resultant 12,288/N average values. A second method used a running average over the set, i.e., when N = 8, the groups averaged are 1–8, 2–9, 3–10, . . . , 12,281–12,288, and the measured standard deviation is then based on the 12,288−N average values. It will be established in the course of this paper that the two methods yield essentially the same results for a sufficiently large data sample.

A comparison of the results obtained by the two methods for the initial set of 12,288 pulses from both laser 1, L_1, and laser 2, L_2, is given in Table I, which shows the measured percentage signal-averaged standard deviation σ_N of the normalized lidar returns as N is increased from 1 to 2048 by factors of 2. Little differences between the two averaging methods is observed for all values of N, with the results essentially identical for N < 256. The corresponding results for the final set of 12,288 pulse returns are given in Table II. The tables also contain the results for the ratio of the pulse pairs; the ratio values are required for differential-absorption lidar measurements (see Appendix A). There is no observable reduction in the standard deviation using the ratios in the initial set, which is consistent with the fact that the measured cross-correlation coefficient of the corresponding pulses from the two lasers was <0.5.[11,12] However, the use of ratios in the final set is seen to lead to a marked reduction in the standard deviation of the mean at large N. This improvement, which occurs despite a pulse-pair cross-correlation coefficient <0.5 (as seen by the lack of improvement at N = 1), has been shown to be due to a slow drift in atmospheric absorption which occurred during the time

Table I. Percentage Standard Deviation of Signal-Averaged Lidar Returns From the Initial Set of 12,288 Pulses

| N | Laser 1 $P(28)$ | | | Laser 2 $P(22)$ | | | Ratio $L1/L2$ | | |
	Running average	Segmental average	Calculated	Running average	Segmental average	Calculated	Running average	Segmental average	Calculated
1	20.5	20.5		17.7	17.7		22.3	22.3	
2	16.7	16.7	16.7	14.7	14.6	14.7	17.0	17.0	17.0
4	13.7	13.8	13.7	12.3	12.2	12.3	13.3	13.3	13.2
8	11.2	11.3	11.2	10.2	10.1	10.3	10.6	10.8	10.7
16	9.0	9.0	9.1	8.4	8.3	8.6	8.8	8.7	8.9
32	7.2	7.3	7.3	7.0	7.0	7.2	7.5	7.6	7.7
64	5.8	6.0	5.8	6.0	6.1	6.2	6.6	6.6	6.8
128	4.6	4.8	4.8	5.2	5.2	5.4	5.8	5.8	6.2
256	3.7	3.8	4.0	4.5	4.5	4.7	4.9	4.9	5.2
512	3.0	3.0	3.0	3.7	3.9	4.0	3.8	4.0	4.3
1024	2.6	2.7	2.3	3.0	3.3	3.2	2.8	3.3	3.3
2048	2.3	2.2	2.6	2.3	2.8	2.4	2.2	2.4	2.6

| N	Laser 1 P(28)			Laser 2 P'(.2)			Ratio L1/L2		
	Running average	Segmental average	Calculated	Running average	Segmental average	Calculated	Running average	Segmental average	Calculated
1	21.7	21.7		18.3	18.3		22.2	22.2	
2	18.0	18.0	18.0	15.2	15.2	15.2	16.8	16.8	16.8
4	15.1	15.1	15.1	12.7	12.7	12.8	12.9	12.9	12.9
8	12.8	12.8	12.9	10.7	10.7	10.9	10.0	10.0	10.0
16	10.9	10.8	11.1	9.1	9.1	9.3	7.9	7.9	8.1
32	9.5	9.5	9.7	7.9	7.8	8.0	6.6	6.4	6.8
64	8.5	8.5	8.6	7.1	7.1	7.1	5.4	5.3	5.7
128	7.9	7.9	8.0	6.6	6.6	6.6	4.5	4.5	4.8
256	7.5	7.5	7.6	6.2	6.0	6.2	3.9	3.9	4.1
512	7.2	7.3	7.2	5.8	5.8	5.9	3.3	3.4	3.5
1024	6.9	7.0	6.9	5.5	5.2	5.6	2.7	2.8	3.1
2048	6.3	6.8	6.5	4.9	4.8	5.3	2.0	2.4	2.3
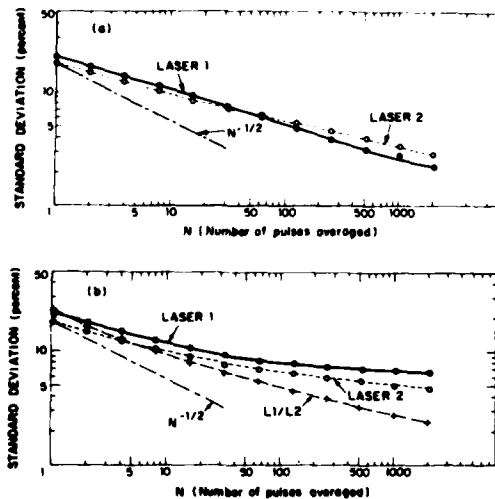
Fig. 1. Measured percentage standard deviation of lidar return signals as a function of the number of pulses averaged: (a) Returns from laser 1 and laser 2 for the initial set of 12,288 pulses; (b) returns from laser 1, laser 2, and their ratio for the final set of 12,288 pulses. The ratio results for the initial set are not shown in (a) as they are essentially the same as those obtained for the individual lasers.

interval encompassed by the final set.[12] The relatively poor pulse-pair cross-correlation obtained from the two lasers, despite the effectively frozen atmosphere during the 50-μsec interval between pulses, is attributable to instrumental effects, specifically a combination of electronic effects, pulse-to-pulse changes in mode quality, and small directional shifts in the laser beams.[7]

The variation of the segmental standard deviation σ_N as a function of N is shown graphically in Fig. 1 for the initial and final sets, respectively. It is seen that in all cases the reduction of σ_N with N is significantly smaller than the $N^{-1/2}$ dependence predicted for independent measurements.

III. Theory

The departure from $N^{-1/2}$ behavior seen in Fig. 1 indicates that the measurements are not truly independent; that is, sucessive pulses are correlated. This behavior can be explained quantitatively by a theoretical analysis which considers the effect of temporal correlation.

To evaluate the temporal correlation of the lidar pulse returns, let us define $I_k = I(t_k)$ as the normalized deviation of the kth pulse return (occurring at time t_k) from its mean value $\overline{P}$ over the full set of data. Then,

$$I_k = \frac{P_k - \overline{P}}{\overline{P}}, \qquad (1)$$

where P_k is the kth lidar pulse return signal. The normalized variance of the full set of individual pulses is defined as

$$\sigma^2 \equiv \langle (I_k)^2 \rangle = \frac{1}{\Gamma} \sum_{k=1}^{\Gamma} I_k^2, \qquad (2)$$

where Γ is the total number of pulses in the set, which is equal to 12,288 in our experiments. The temporal autocorrelation coefficient ρ_j for a delay time equal to $j\tau$ is then given by

$$\rho_j = \frac{1}{\sigma^2} \langle I(t_k)I(t_k + j\tau) \rangle = \frac{1}{\sigma^2(\Gamma - j)} \sum_{k=1}^{\Gamma-j} I_k I_{k+j}, \qquad (3)$$

where τ is the time interval between pulses These definitions of ρ_j and σ^2 are independent of the probability-distribution function of the signals.

Equation (3) was used to calculate the correlation coefficient ρ_j for $j = 1,2,4,8,\ldots,1024,2048$, using the lidar pulse returns from L_1, L_2, and L_1/L_2. The results are given in Fig. 2 for the initial and final sets of data, respectively. It is seen from the figures that small positive temporal correlations persist in the first set out of 10 sec and beyond, while the presence of a slow drift in the atmospheric absorption during the final set[12] is seen to result in a larger positive correlation which persists beyond 200 sec in the lidar returns.

29

Previous studies of the temporal correlation coefficient for backscattered CO_2 laser radiation through the atmosphere from a hard target have indicated that the atmosphere is effectively frozen for the order of 1–5 msec, with a significant drop in correlation by 50–100 msec.[7][13] However, residual positive correlation has been observed to persist out to several seconds.[8]

The short-term correlation is primarily due to turbulence caused by thermal fluctuations in the atmosphere.[14] For temporal correlations over the longer time intervals considered in this paper, changes in absorption due to humidity fluctuations appear to play a significant role.[12] The resultant temporal autocorrelation as given in Fig. 2 represents the summed effect of all the time constants involved, including those mentioned above.

To establish if the temporal correlation levels shown in Fig. 2 are sufficient to cause the strong reduction in the effectiveness of pulse averaging relative to $N^{-1/2}$ behavior as shown in Fig. 1, the relationship between σ_N and ρ_j was derived for both the segmental- and running-average approaches. The theoretical analysis for segmental averaging is given in Appendix B and leads to the relationship

$$\sigma_N(\text{seg}) = \frac{\sigma}{\sqrt{N}}\left[1 + 2\sum_{j=1}^{N-1}(1 - j/\Gamma)(1 - j/N)\rho_j\right]^{1/2}. \quad (4)$$

Using a running average of the lidar returns, the relationship is shown in Appendix C to be

$$\sigma_N(\text{run}) = \frac{\sigma}{\sqrt{N}}\left[1 + 2\sum_{j=1}^{N-1}(1 - j/N)\rho_j\right]^{1/2}. \quad (5)$$

It should be noted that in the absence of correlation ($\rho_j = 0$), Eqs. (4) and (5) predict the expected $N^{-1/2}$

Fig. 2. Autocorrelation coefficient of lidar return signals from laser 1, laser 2, and their ratio as a function of time delay between signals based on a 10-Hz pulse-repetition rate: (a) Initial set of 12,288 pulses; (b) final set of 12,288 pulses.

dependence. It is shown in Appendix B that Eq. (5) is an excellent approximation to Eq. (4), so this simpler form can be used for both segmental- and running-average calculations. This effective near-equivalence of $\sigma_N(\text{seg})$ and $\sigma_N(\text{run})$ accords with the agreement observed experimentally, as seen in Tables I and II.

Values for σ_N were calculated on the basis of Eq. (5), using the values of ρ_j given in Fig. 2 for $j = 1,2,4,8,\ldots$, 1024,2048, and assuming a linear interpolation for all other values of j. The results of the calculation are included in Tables I and II. The agreement between the calculated and the measured values of σ_N is seen to be excellent even at large N values, where the assumptions of equal weighting (discussed in Appendices B and C) and the linear interpolation of ρ_j values are weakest. This agreement effectively validates these assumptions and shows that the presence of small but persistent temporal correlation severely limits the improvement available through signal averaging of lidar returns from hard targets.

It should be noted that the process considered in the above analysis is almost certainly not stationary on the time scale of the experiments and is definitely not Markovian, since the autocorrelation function always decays exponentially in Markovian processes.[15,16] Most theoretical work is concerned strictly with stationary processes,[17] and much of it is concerned with Markovian processes. The work presented here is subject to neither of these limitations.

IV. Data Analysis

To establish the relative contribution to σ_N of the short-term and the long-term autocorrelation coefficients, Eq. (5) has been evaluated assuming (1) ρ_j equals a constant, $\rho_j = \rho$; (2) ρ_j decreases logarithmically with increasing j, $\rho_j = A - B\ln(j)$; and (3) ρ_j decreases exponentially, $\rho_j = \exp(-j\alpha)$. The evaluation for each of these three assumed functional relationships of ρ_j is given in Appendix D.

For the case of a constant value $\rho_j = \rho$, Eq. (D2) shows that in the limit for large values of N

$$\sigma_N \approx \sigma\sqrt{\rho}. \quad (6)$$

This situation is approximated experimentally when there is a continuous atmospheric drift throughout the measurement period, as was the case during the final set of data taken with lasers 1 and 2 as seen in Fig. 1(b). As an example, using $\sigma = 0.22$ from Fig. 1(b) and $\rho = 0.05$ from Fig. 2(b), substitution into Eq. (6) leads to $\sigma_N \sim$ 0.05. This result is consistent with the experimental data shown in Fig. 1(b) and indicates that improvement in the standard deviation of the mean is limited in this case to a factor of $\sim$4, independent of the number of pulses averaged.

A more accurate approximation to the experimental results can be obtained by noting in Fig. 2 that there is an initial rapid decrease in ρ_j, followed by a ρ_j value which decreases slowly with increasing j. This behavior can be approximated reasonably by a model which assumes ρ_j to be the sum of an exponential term and a
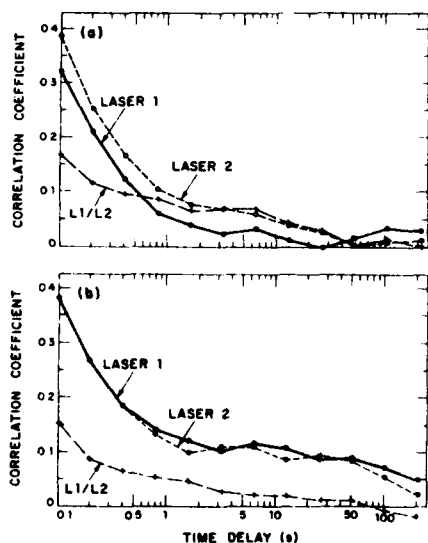
30

logarithmically decreasing term as described in Appendix D.

A value of α is chosen such that the exponential term $\rho_j = \exp(-j\alpha)$ is the dominant contributor to σ_N at small values of j, but its contribution becomes negligible by $j > 16$. Beyond this value, the effect of the exponential term alone on σ_N would be approximated by Eq. (D7), where it is shown that σ_N at the larger values of N will be increased by the constant factor $[\coth(\alpha/2)]^{1/2}$ over the noncorrelated case but exhibits an $N^{-1/2}$ dependence. The failure of σ_N to achieve this $N^{-1/2}$ dependence is due to the presence of the logarithmically decreasing term $\rho_j = A - B \ln(j)$. For the larger values of N in Fig. 1, the resulting σ_N values are then almost entirely due to a term of this form.

These effects are illustrated in Fig. 3, which shows the values of σ_N obtained by applying Eq. (5) for $\rho_j = \exp(-j\alpha)$, $\rho_j = A - B \ln(j)$, and $\rho_j = \exp(-j\alpha) + A - B \ln(j)$, where $\alpha = 0.693$, $A = 0.14$, and $B = 0.02$. The values of A and B were chosen to reasonably approximate the values of ρ_j at high j shown for laser 2 in Fig. 2(a). The value of α was chosen such that $\exp(-\alpha) = 0.5$, which approximates the experimental data. The resulting σ_N curves in Fig. 3 are of the proper magnitude compared with the experimental results in Fig. 2 and show that the standard deviation after signal averaging over a large number of pulses is primarily due to the long-term correlation from $A - B \ln(j)$.

In determining the extent to which remote-sensing accuracy can be improved by increasing the number of data points, it should be noted that if ρ is any monotonically decreasing or constant function of delay time,

$$\sigma_N \geq \sigma \sqrt{\rho_{N-1}}. \tag{7}$$

This is shown in Appendix D to be true for a constant correlation coefficient (i.e., $\rho_j = \rho = \rho_{N-1}$). Therefore, to prove the statement, it is only necessary to note that

$$\sigma_N = \frac{\sigma}{\sqrt{N}} \left[1 + 2 \sum_{j=1}^{N-1} (1 - j/N)\rho_j \right]^{1/2}$$
$$\geq \frac{\sigma}{\sqrt{N}} \left[1 + 2 \sum_{j=1}^{N-1} (1 - j/N)\rho_{N-1} \right]^{1/2}, \tag{8}$$

since, by definition of the correlation coefficient as a monotonically decreasing or constant function of delay time, $\rho_j \geq \rho_{N-1}$ for all $j \leq N - 1$.

Equation (7) represents a fundamental inequality which can impose a severe limitation on the improvement attainable by averaging over a large sample. As long as the monotonically decreasing temporal correlation coefficient, ρ_{N-1}, has a finite value for a given time interval, that value limits the improvement in the standard deviation that can be obtained by signal averaging regardless of the number of pulses averaged during that interval. For example, in the time interval required to bring the temporal correlation coefficient down to 1%, it is impossible for signal averaging to achieve more than a tenfold reduction in the standard deviation. It should further be noted that this degree of improvement occurs only for a constant correlation

coefficient. For a decreasing ρ_j, the improvement can be significantly smaller.

It is apparent from the above considerations that very small temporal correlation values can severely limit the improvement achievable by signal averaging. This can be an important factor since our experimental data indicates that such small correlation values may persist over long time intervals, at least for lidar returns from a stationary target.

Appendix A. Application to DIAL Measurements

The use of DIAL measurements to determine the concentration of gaseous species in the atmosphere requires determination of the ratio of the average value of lidar returns P and P' at two different wavelengths. The accuracy in the measurement of this ratio, P/P', has been shown[11] to be related approximately to the accuracy of each single lidar measurement as

$$\sigma_{P/P'}^2 = \sigma_P^2 + \sigma_{P'}^2 - 2\rho_0 \sigma_P \sigma_{P'}, \tag{A1}$$

where $\sigma_{P/P'}$, σ_P, and $\sigma_{P'}$ are the normalized standard deviations of the measurement of P/P', P, and P', respectively, and ρ_0 is the temporal pulse-pair cross-correlation coefficient of the individual P_k and P'_k lidar measurements.[8,11] As seen in Eq. (A1), if $\rho_0 = 0$, then $\sigma_{P/P'}^2 = \sigma_P^2 + \sigma_{P'}^2$; if $\rho_0 \sim 1$, then $\sigma_{P/P'}^2$ is significantly reduced in value. As $\sigma_{P/P'}$ is a measure of the accuracy of a DIAL measurement, the presence of a large temporal cross correlation leads to a significant improvement in this measurement accuracy relative to DIAL experiments obtained with a system in which the measurement at the two frequencies is not made within the correlation time.

Since the effect of signal averaging is to operate on both sides of Eq. (A1) with $(1/T)\int dt$, these results may also be applied directly to signal-averaged DIAL measurements. In this case, $\sigma_{P/P'}$, σ_P, and $\sigma_{P'}$ in Eq. (A1) become the values of the signal-averaged standard deviation of the mean as calculated in Eqs. (4) and (5), and ρ_0 is the temporal cross correlation coefficient of the signal-averaged values. An example of the application of Eq. (A1) using signal-averaged values was presented in Ref. 12, where excellent agreement between calculated results and experimental data was obtained.

Appendix B. Segmental Averaging

The variance of the Γ lidar returns which have been segmentally averaged over N returns is defined by

$$\sigma_N^2 = \frac{1}{\Gamma/N} \left[\left(\frac{I_1 + I_2 + \ldots + I_N}{N} \right)^2 + \left(\frac{I_{N+1} + \ldots + I_{2N}}{N} \right)^2 + \ldots + \left(\frac{I_{\Gamma-(N-1)} + \ldots + I_\Gamma}{N} \right)^2 \right]. \tag{B1}$$
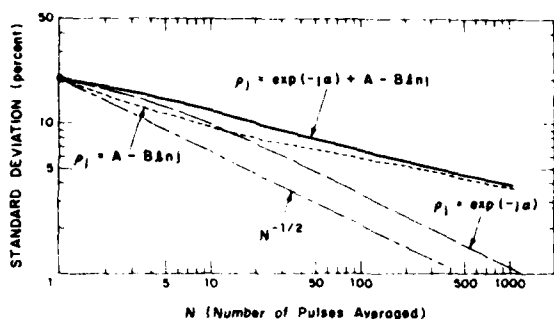
Expanding Eq. (B1) leads directly to

Fig. 3. Calculated percentage standard deviation as a function of the number of pulses averaged for $\rho_j = \exp(-j\alpha)$, $\rho_j = A - B \ln(j)$, and their sum, where $\alpha = 0.693$, $A = 0.14$, $B = 0.02$, and $\sigma = 0.2$.

$$\sigma_N^2 = \frac{1}{N\Gamma} \{(I_1^2 + I_2^2 + \ldots + I_\Gamma^2) + 2\{(I_1 I_2 + I_2 I_3 + \ldots + I_{N-} I_N)$$

$$+ (I_{N+1}I_{N+2} + \ldots + I_{2N-1}I_{2N}) + \ldots + (I_{\Gamma-(N-1)}I_{\Gamma-(N-2)} + \ldots + I_{\Gamma-1}I_\Gamma\}$$

$$+ 2\{(I_1 I_3 + I_2 I_4 + \ldots + I_{N-2}I_N) + (I_{N+1}I_{N+3} + \ldots + I_{2N-2}I_{2N}) + \ldots$$

$$+ (I_{\Gamma-(N-1)}I_{\Gamma-(N-3)} + \ldots + I_{\Gamma-2}I_\Gamma)\} + \ldots$$

$$+ 2\{(I_1 I_N) + (I_{N+1}I_{2N}) + \ldots + (I_{\Gamma-(N-1)}I_\Gamma)\}\}. \qquad (B2)$$

From the definition of the variance σ^2 as given in Eq. (2), the first set of terms in parentheses on the right-hand side of Eq. (B2) is just $\Gamma\sigma^2$. Within each curly bracket the terms in parentheses are cross-product terms obtained from the corresponding parentheses in Eq. (B1), and the curly brackets have been arranged such that the sets of terms in the jth bracket are related to the jth correlation coefficient ρ_j [see Eq. (3)]. In general, the relationship would be equal to $(\Gamma - j)\sigma^2\rho_j$, except that the fractional number j/N of the terms are missing. These arise from the absence of cross-product terms between parentheses; i.e., for $j = 1$, the terms $I_N I_{N+1}, I_{2N}I_{2N+1}$, etc. are missing. If we assume that the missing interpolated terms have the same average value as the terms present, Eq. (B2) can be rewritten as

$$\sigma_N^2 = \frac{1}{N\Gamma}\left(\sigma^2\Gamma + 2\sigma^2\left\{\left(\frac{N-1}{N}\right)(\Gamma - 1)\rho_1\right.\right.$$

$$+ \left(\frac{N-2}{N}\right)(\Gamma - 2)\rho_2 + \ldots$$

$$\left.\left. + \frac{1}{N}\{\Gamma - (N-1)\rho_{N-1}\}\right]\right), \qquad (B3)$$

or

$$\sigma_N^2 = \frac{\sigma^2}{N}\left[1 + 2\sum_{j=1}^{N-1}(1 - j/N)(1 - j/\Gamma)\rho_j\right]. \qquad (B4)$$

The assumption of equal average weighting for the interpolated terms appears reasonable given the well-behaved temporal correlation behavior shown in Fig. 2. The ultimate validation for this assumption lies in the agreement between Eq. (B4) and the experimental results given in Tables I and II.

It can be shown, assuming $\rho_j = $ constant, that the fractional error introduced by ignoring the term $(1 - j/\Gamma)$ in Eq. (B4) is approximately equal to $N/3\Gamma$. In the experiments considered in this paper, $\Gamma = 12,288$; therefore, for small N the fractional error is negligibly small. For the worst cases considered, $N = 1024$ and 2048, the fractional errors would be slightly <3% and 6%, respectively. However, these represent an overestimate of the errors, since ρ_j is not a constant but, rather, a decreasing function of j. Therefore, to a good approximation, Eq. (B4) can be further simplified to the form

$$\sigma_N^2 = \frac{\sigma^2}{N}\left[1 + 2\sum_{j=1}^{N-1}(1 - j/N)\rho_j\right]. \qquad (B5)$$

Appendix C.   Running Averaging

The variance of the Γ lidar returns for a running average over N returns is defined by

$$\sigma_N^2 = \frac{1}{\Gamma - (N-1)}\left[\left(\frac{I_1 + I_2 + \ldots + I_N}{N}\right)^2 + \left(\frac{I_2 + I_3 + \ldots + I_{N+1}}{N}\right)^2 + \ldots + \left(\frac{I_{\Gamma-(N-1)} + \ldots + I_\Gamma}{N}\right)^2\right] \qquad (C1)$$

$$= \frac{1}{N^2[\Gamma - (N-1)]}\{\{(I_1^2 + I_2^2 + \ldots + I_\Gamma^2) + (I_2^2 + I_3^2 + \ldots + I_{\Gamma-1}^2) + \ldots + (I_N^2 + I_{N+1}^2 + \ldots + I_{\Gamma-(N-1)}^2)\}$$

$$+ 2\{(I_1 I_2 + I_2 I_3 + \ldots + I_{\Gamma-1}I_\Gamma) + (I_2 I_3 + \ldots + I_{\Gamma-2}I_{\Gamma-1}) + \ldots + (I_{N-1}I_N + \ldots + I_{\Gamma-(N-1)}I_{\Gamma-(N-2)})\}$$

$$+ 2\{(I_1 I_3 + I_2 I_4 + \ldots + I_{\Gamma-2}I_\Gamma) + (I_2 I_4 + \ldots + I_{\Gamma-3}I_{\Gamma-1}) + \ldots + (I_{N-2}I_N + \ldots + I_{\Gamma-(N-1)}I_{\Gamma-(N-3)})\}$$

$$+ \ldots 2\{(I_1 I_N + I_2 I_{N+1} + \ldots + I_{\Gamma-(N-1)}I_\Gamma)\}\}. \qquad (C2)$$

The set of terms in the first parentheses of the first curly bracket on the right-hand side of Eq. (C2) is equal to $\Gamma\sigma^2$, and each succeeding set in the bracket is similar but with the first and last term of the preceding set eliminated. The first set of terms in the jth succeeding curly bracket is similarly related to the correlation function ρj, being equal to $(\Gamma - j)\sigma^2\rho j$, with succeeding sets again dropping the outer terms. As in Appendix B, we assume that the missing terms have the same average value as the terms present. In Appendix B the missing terms were interpolated ones; here the situation is reversed, with the central terms present and the missing terms obtained by extrapolation at both ends. With the equal weighting assumption, Eq. (C2) becomes

32

$$\sigma_N^2 = \frac{1}{N^2[\Gamma - (N-1)]} \left\{ \sigma^2[\Gamma + (\Gamma - 2) + (\Gamma - 4) + \ldots + [\Gamma - 2(N-1)]] \right.$$
$$+ 2\rho_1\sigma^2[(\Gamma - 1) + (\Gamma - 3) + \ldots + [\Gamma - 2(N-1) + 1]]$$
$$+ 2\rho_2\sigma^2[(\Gamma - 2) + (\Gamma - 4) + \ldots + [\Gamma - 2(N-1) + 2]]$$
$$\left. + \ldots + 2\rho_{N-2}\sigma^2\{[\Gamma - (N-2)] + (\Gamma - N)\} + 2\rho_{N-1}\sigma^2\{\Gamma - (N-1)\} \right\}. \tag{C3}$$

Since $\Gamma - 2(N-1) + k \equiv (\Gamma - k) - 2[N - (k+1)]$,
we obtain

$$\sigma_N^2 = \frac{\sigma^2}{N^2[\Gamma - (N-1)]} \left[\sum_{i=0}^{N-1} (\Gamma - 2i) + 2\rho_1 \sum_{i=0}^{N-2} [(\Gamma - 1) - 2i] + 2\rho_2 \sum_{i=0}^{N-3} [(\Gamma - 2) - 2i] \right.$$
$$\left. + \ldots + 2\rho_{N-2} \sum_{i=0}^{1} [\Gamma - (N-2) - 2i] + 2\rho_{N-1}[\Gamma - (N-1)] \right]. \tag{C4}$$

Evaluating the summations yields

$$\sigma_N^2 = \frac{\sigma^2}{N^2[\Gamma - (N-1)]} \left\{ N[\Gamma - (N-1)] + 2\rho_1(N-1)[\Gamma - (N-1)] + 2\rho_2(N-2)[\Gamma - (N-1)] \right.$$
$$\left. + \ldots + 2\rho_{N-2} \times 2[\Gamma - (N-1)] + 2\rho_{N-1}[\Gamma - (N-1)] \right\}. \tag{C5}$$

Therefore,

$$\sigma_N^2 = \frac{\sigma^2}{N} \left[1 + \frac{2}{N} \sum_{j=1}^{N-1} (N - j)\rho_j \right], \tag{C6}$$

or,

$$\sigma_N^2 = \frac{\sigma^2}{N} \left[1 + 2 \sum_{j=1}^{N-1} (1 - j/N)\rho_j \right]. \tag{C7}$$

The above relationship between the correlation coefficient and the pulse-averaged variance for a running average differs from the relationship obtained for segmental averaging, which is given in Eq. (B4). However, as was discussed in Appendix B, the difference is quantitatively small, and the approximate form for segmental averaging as given in Eq. (B5) is identical with Eq. (C7).

Appendix D.   Analytic Correlation Functions

In this Appendix we investigate the pulse-averaged variance of the mean as a function of the number of pulses averaged for three different correlation coefficients, ρ_j, which are analytic functions of j. These analytic functions are used in Eq. (5) to calculate σ_N^2

(1) $\rho_j = \text{constant} = \rho$:

$$\rho \sum_{j=1}^{N-1} (1 - j/N) = \rho \left\{ (N-1) - \frac{1}{N} \left[\frac{N(N-1)}{2} \right] \right\} = \rho \frac{(N-1)}{2}, \tag{D1}$$

$$\therefore \sigma_N^2 = \frac{\sigma^2}{N} [1 + \rho(N-1)]. \tag{D2}$$

For $\rho N \gg 1$, $\sigma_N^2 \approx \sigma^2 \rho$.

(2) $\rho_j = \exp(-j\alpha)$:

References

1. J. W. Strohbehn, Ed., *Laser Beam Propagation in the Atmosphere* (Springer, New York, 1978).
2. R. L. Fante, Radio Sci. **15**, 757 (1980).
3. J. C. Leader, J. Opt. Soc. Am. **71**, 542 (1981).
4. J. W. Goodman, Proc. IEEE **53**, 1688 (1965).
5. M. H. Lee and J. F. Holmes, J. Opt. Soc. Am. **71**, 559 (1981).
6. J. H. Shapiro, B. A. Capron, and R. C. Harney, Appl. Opt. **20**, 3292 (1981).
7. N. Menyuk and D. K. Killinger, Opt. Lett. **6**, 301 (1981).
8. D. K. Killinger and N. Menyuk, IEEE J. Quantum Electron. **QE-17**, 1917 (1981).
9. N. Menyuk and P. F. Moulton, Rev. Sci. Instrum. **51**, 216 (1980).
10. R. A. McClatchey, R. W. Fenn, J. E. A. Selby, F. E. Volz, and J. S. Garing, "Optical Properties of the Atmosphere" Report AFCRL-72-0497, Environmental Research Paper No. 411, (1972).
11. D. K. Killinger and N. Menyuk, Appl. Phys. Lett. **38**, 968 (1981).
12. N. Menyuk, D. K. Killinger, and W. E. DeFeo, Appl. Opt. **21**, 2275 (1982).
13. B. Marthinsson, J. Johansson, and S. T. Eng, Opt. Quantum Electron. **12**, 327 (1980).
14. R. J. Hill, S. F. Clifford, and R. S. Lawrence, J. Opt. Soc. Am. **70**, 1192 (1980).
15. J. L. Doob, *Stochastic Properties* (Wiley, New York, 1953).
16. P. A. Pincus, R. A. Elliot, and J. R. Kerr, J. Opt. Soc. Am. **68**, 756 (1978).
17. Y. A. Yaglom, *An Introduction to the Theory of Stationary Random Functions* (Prentice-Hall, Englewood Cliffs, N.J., 1962).

$$\sum_{j=1}^{N-1} (1 - j/N) \exp(-j\alpha) = \frac{\exp(-\alpha)}{N[1 - \exp(-\alpha)]^2} \{N[1 - \exp(-\alpha)] - [1 - \exp(-N\alpha)]\},$$

$$\therefore \sigma_N^2 = \frac{\sigma^2}{N} \left(1 + \frac{2\exp(-\alpha)}{N[1 - \exp(-\alpha)]^2} \{N[1 - \exp(-\alpha)] - [1 - \exp(-N\alpha)]\} \right). \tag{D3}$$

or,

$$\sigma_N^2 = \frac{\sigma^2}{N} \left[\frac{N[1 - \exp(-2\alpha)] - 2\exp(-\alpha)[1 - \exp(-N\alpha)]}{N[1 - \exp(-\alpha)]^2} \right]. \tag{D4}$$

For $N \gg 1$ and $\exp(-N\alpha) \ll 1$

$$\sigma_N^2 \approx \frac{\sigma^2}{N} \frac{[1 + \exp(-\alpha)]}{[1 - \exp(-\alpha)]} = \frac{\sigma^2}{N} \coth(\alpha/2). \tag{D5}$$

(3) $\rho_j = A - B \ln j$: \hfill (D6)

$$\sum_{j=1}^{N-1} (1 - j/N)(A - B \ln j) = \frac{A}{2}(N-1) - B \sum_{j=1}^{N-1} (1 - j/N) \ln j,$$

$$\therefore \sigma_N^2 = \frac{\sigma^2}{N} \left[1 + A(N-1) - 2B \sum_{j=1}^{N-1} (1 - j/N) \ln j \right].$$

REPORT DOCUMENTATION PAGE		READ INSTRUCTIONS BEFORE COMPLETING FORM
1. REPORT NUMBER ESD-TR-83-018 ESL-TR-83-029	2. GOVT ACCESSION NO. AD - A130 257	3. RECIPIENT'S CATALOG NUMBER
4. TITLE (and Subtitle) Laser Remote Sensing of Atmospheric Pollutants		5. TYPE OF REPORT & PERIOD COVERED Final Report 1 October 1981 — 30 September 1982
		6. PERFORMING ORG. REPORT NUMBER
7. AUTHOR(s) Dennis K. Killinger, Norman Menyuk, Aram Mooradian		8. CONTRACT OR GRANT NUMBER(s) F19628-80-C-0002
9. PERFORMING ORGANIZATION NAME AND ADDRESS Lincoln Laboratory, M.I.T. P.O. Box 73 Lexington, MA 02173-0073		10. PROGRAM ELEMENT, PROJECT, TASK AREA & WORK UNIT NUMBERS Program Element No. 62601F Project No. 1900
11. CONTROLLING OFFICE NAME AND ADDRESS Engineering and Services Laboratory Air Force Engineering and Services Center Tyndall AFB, FL 32403		12. REPORT DATE 30 September 1982
		13. NUMBER OF PAGES 38
14. MONITORING AGENCY NAME & ADDRESS (if different from Controlling Office) Electronic Systems Division Hanscom AFB, MA 01731		15. SECURITY CLASS. (of this report) Unclassified
		15a. DECLASSIFICATION DOWNGRADING SCHEDULE

16. DISTRIBUTION STATEMENT (of this Report)

Approved for public release; distribution unlimited.

17. DISTRIBUTION STATEMENT (of the abstract entered in Block 20, if different from Report)

18. SUPPLEMENTARY NOTES

None

19. KEY WORDS (Continue on reverse side if necessary and identify by block number)

laser remote sensing	mini-TEA CO_2 laser
environmental monitoring	LIDAR (DIAL) system
tactical detection and discrimination	remote detection of CO, NO, C_2H_4, hydrazine MMH and UDMH

20. ABSTRACT (Continue on reverse side if necessary and identify by block number)

    This is the FY 82 final report on the program entitled "Laser Remote Sensing of Atmospheric Pollutants" supported by the Air Force Engineering and Services Center (AFESC).

    The specific tasks which were conducted during FY82 for this research program consisted of the following: (1) the initial development of a heterodyne-detection, differential-absorption LIDAR (DIAL) system, (2) the development of a computerized data acquisition and processing system for range-resolved, heterodyne-detection DIAL measurements, (3) preliminary range-resolved, heterodyne-detection DIAL measurements of atmospheric species, and (4) a study of the potential application of the continuously tunable Co:MgF_2 IR laser for remote sensing of airfield pollutants and gaseous species.

DD FORM 1473 EDITION OF 1 NOV 65 IS OBSOLETE
1 Jan 73

8